PNAS
www.pnas.org

Supplementary Information for

The structural bases for agonist diversity in an *Arabidopsis thaliana* glutamate receptor-like channel

Andrea Alfieri, Fabrizio G. Doccula, Riccardo Pederzoli, Matteo Grenzi, Maria Cristina Bonza, Laura Luoni, Alessia Candeo, Neli Romano Armada, Alberto Barbiroli, Gianluca Valentini, Thomas R. Schneider, Andrea Bassi, Martino Bolognesi, Marco Nardini, Alex Costa.

Corresponding authors: Andrea Alfieri (email: andrea.alfieri@unimi.it), Alex Costa (email: alex.costa@unimi.it)

This PDF file includes:

www.pnas.org/cgi/doi/10.1073/pnas.1905142117

SUPPLEMENTARY DATA

To strengthen the evidence that binding of amino acids to GLRs underlies the $[Ca^{2+}]_{cyt}$ increase, we studied at high spatial resolution, by means of light sheet fluorescence microscopy (LSFM), the amino acid-elicited $[Ca^{2+}]_{cyt}$ dynamics in *Arabidopsis* root tip cells of Col-0 plants expressing the genetically-encoded Ca^{2+} sensor NES-YC3.6 (1–3) (*SI Appendix*, Figs. S2A and S3). The rationale behind the choice of the seven analyzed amino acids (*SI Appendix*, Fig. S3) was based on the current literature (4, 5) and on experiments in which we evaluated, by means of FRET-based wide-field fluorescence microscopy analyses, the $[Ca^{2+}]_{cyt}$ transients in *Arabidopsis* root tip in response to the L-enantiomers of all 20 amino acids (administered at 1 mM final concentration) (*SI Appendix*, Fig. S4). The wide-field experiments revealed that only L-Cys, L-Glu, L-Ala, Gly, L-Ser, L-Asn and, to minor extent, L-Met were able to trigger $[Ca^{2+}]_{cyt}$ increases in root tip cells (L-Met evoked a small but clear FRET signal, that was not detected for any of the remaining 13 amino acids) (*SI Appendix*, Figs. S2*E* and S4). These results confirm those previously obtained in *Arabidopsis* with an earlier Cameleon version and/or aequorin-expressing plants (4, 6). Importantly, the use of LSFM offered the necessary resolution to affirm that the $[Ca^{2+}]_{cyt}$ transients evoked by the seven different amino acids occurred primarily in the lateral cells of the root meristem and only later spread towards the inner cells of the stele (*SI Appendix*, Figs. S2*A*, *B* and S3).

The GLR3.3 was shown to be required for the amino acid-induced $[Ca^{2+}]_{cyt}$ increase and PM depolarization in *Arabidopsis* seedlings (4, 6, 7). We thus analysed the GLR3.3 expression pattern in *Arabidopsis* seedlings root tip cells through confocal analysis of plants expressing the GLR3.3-EGFP fusion protein under the control of the GLR3.3 promoter (8) (*SI Appendix*, Fig. S2*C*, *C'*). A close inspection of the GLR3.3 subcellular localization showed an apparent accumulation of the protein at the basal and apical membranes, but also intracellular punctate assemblies reminiscent of the endomembrane system (*SI Appendix*, Fig. S2*C'*) which may include the endoplasmic reticulum (ER). Such a hypothesis is supported by the presence of GLR3.3 in the ER of phloem sieve elements (9). Thus our, and previous, results suggest that GLR3.3 might be subjected to a fine subcellular sorting, as reported in pollen (10) and also for animal AMPARs (11). Indeed, the precise regulation of GLR3.3 subcellular localization in root tip cells will require additional investigations, bearing in mind that the GFP tag might affect the *in vivo* subcellular localization of the channel. Nevertheless, a side by side comparison of the GLR3.3-EGFP fluorescence signal with the LSFM Ca^{2+} imaging (*SI Appendix*, Fig. S2*A*, *C*) demonstrated that the GLR3.3 is expressed in those cells where the amino acids-induced Ca^{2+} transients occur. To unequivocally prove that GLR3.3 is involved in the amino acid-induced $[Ca^{2+}]_{cyt}$ increases in root tip cells, we expressed the NES-YC3.6 sensor in two different *GLR3.3* T-DNA lines (*glr3.3-1* and *glr3.3-2*) (4, 6, 7). The comparison of resting Ca^{2+} levels by means of wide-field fluorescence microscopy in root tip cells revealed no difference between the wild-type and mutant alleles (*SI Appendix*, Fig. S2*D*). Nonetheless, the lack of GLR3.3 completely prevented any amino acid-induced $[Ca^{2+}]_{cyt}$ increase assayed by means of wide-field fluorescence microscopy, whereas the response to external ATP was not affected (*SI Appendix*, Fig. S2*E*, *F*). These results confirm previous observations that GLR3.3 is required for the amino acid response (4, 6, 7) and that it might be also directly involved in the generation of the $[Ca^{2+}]_{cyt}$ transients.

To assess GLR3.3 Ca^{2+} permeability *in vivo*, we expressed it in the yeast low-affinity Ca^{2+} uptake-deficient triple mutant K667, which lacks the vacuolar ATPase (PMC1), the vacuolar exchanger (VCX1) and the cytosolic regulatory subunit (CNB1) (12–14). Remarkably, the expression of GLR3.3 in the K667 triple mutant complemented the reduced growth of yeast cells at high external $[Ca^{2+}]$

(*SI Appendix*, Fig. S5), hence supporting its direct role in Ca^{2+} transport, as previously suggested by electrophysiological data obtained in mammalian COS-7 cells (10).

MATERIALS AND METHODS

Plant material and growth conditions. All *A. thaliana* plants were of the ecotype Columbia 0 (Col-0). Plants were grown on soil under short day conditions (12 h light /12 h dark, 100 µE m^{-2} s^{-1} of Cool White Neon lamps) at 22 °C and 75% relative humidity. Seeds were surface-sterilized by vapor-phase sterilization (15) and plated on half-strength MS medium (16) (Duchefa) supplemented with 0.1% sucrose, 0.05% MES, pH 5.8, and 0.8% plant agar (Duchefa). After stratification at 4 °C in the dark for 2 days, plates were transferred to the growth chamber under long day conditions (16 h light/8 h dark, 100 µE m^{-2} s^{-1} of Cool White Neon lamps) at 22 °C. For wide-field imaging the plates were kept vertically and the seedlings were used 6-7 days after germination. For light sheet fluorescence microscopy (LSFM) imaging the plates were kept horizontally for 36 hours and the germinated seeds transferred to the Fluorinated Ethylene Propylene tubes (FEP, Adtech FT2x3) as reported in (3).

Generation of transgenic plants. Plant transformation of *glr3.3-1* and *glr3.3-2* T-DNA homozygous mutant alleles (4) with NES-YC3.6 (1) was carried out using *Agrobacterium tumefaciens* GV3101 cells by floral-dip (15). At least two independent transgenic lines for both alleles were selected based on the presence of Cameleon fluorescence using a stereo microscope equipped with a GFP filter. To confirm the presence of T-DNA insertions in homozygosity in the *glr3.3-1* x NES-YC3.6 and *glr3.3-2* x NES-YC3.6 we followed the genotyping strategy reported in (4).

Confocal laser scanning microscopy. Confocal microscopy analyses were performed using a Nikon Eclipse Ti2 inverted microscope, equipped with a Nikon A1R+ laser scanning device (Nikon). EGFP was excited with the 488 nm laser and the emission was collected at 525-550 nm. Images were acquired by a CFI Apo LWD 40x WI (N.A. 1.25) and analyzed using FIJI software (https://fiji.sc/).

Wide-field fluorescence microscopy. For wide-field Ca^{2+} imaging analyses in *Arabidopsis* root tip cells, an inverted fluorescence Nikon microscope (Ti-E) with a 20x(N.A. 0.75) was used. Excitation light was produced by a fluorescent lamp (Prior Lumen 200 PRO, Prior Scientific) set to 20% with 440 nm (436/20 nm) excitation for the Cameleon (YC3.6) sensor. Images were collected with a Hamamatsu Dual CCD camera (ORCA-D2). The FRET CFP/YFP optical block A11400-03 (emission 1, 483/32 nm for CFP; emission 2, 542/27 nm for FRET) with a dichroic 510-nm mirror (Hamamatsu) was used for the simultaneous CFP and cpVenus acquisitions. Camera binning was set to 2 x 2 and exposure times (from 100 to 200 ms) were adjusted depending on the sensor line. Images where acquired every 5 s. Filters and dichroic mirrors were purchased from Chroma Technology. NIS-Elements™ (Nikon) was used as a platform to control the microscope, illuminator, and camera. Images were analyzed using FIJI.

Root tip seedling wide-field fluorescence Ca^{2+} imaging. Seven-day-old seedlings were used for root Ca^{2+} imaging. Seedlings were kept in the growth chamber until the experiment, then were gently removed from the plate according to (17), placed in the dedicated chambers and overlaid with cotton wool soaked in imaging solution (5 mM KCl, 10 mM MES, 10 mM $CaCl_2$ pH 5.8 adjusted with TRIS). The root was continuously perfused with imaging solution while the shoot was not submerged. Treatments were carried out by supplementing the imaging solution with 1 mM of different amino acids (or with lower concentrations where otherwise indicated) or 0.1 mM Na_2ATP (sodium adenosine triphosphate) (from a 200 mM stock solution buffered at pH 7.4 with NaOH) and administered for 3 min under running perfusion.

Light sheet fluorescence microscopy imaging of root tip (LSFM). For LSFM Ca^{2+} imaging analyses in *Arabidopsis* root tip cells a custom-made setup was used (3, 18). The optical path starts with a single-

mode fibre, coupled to a laser emitting at 442 nm (MDL-III-442, CNI), collimated and focalized through a cylindrical lens (f_{CL} = 50 mm) in a horizontal plane. A 1× telescope (f_1 = f_2 = 50 mm, Thorlabs) conjugates the focal plane of the cylindrical lens to the back focal plane of a 10× water-dipping microscope objective (N.A. 0.3, UMPLFLN 10xW, Olympus), which creates a a vertical light-sheet at the sample level. The light sheet is matched to the field of view of a detection objective (N.A. 0.5, UMPLFLN 20xW, Olympus) held orthogonally to the excitation axis. For the detection of the FRET cpVenus/CFP ratio, a two-wavelength detection is required. Thanks to the vertical geometry of plant roots, it is practical to record two images with different spectral content on the same detector by splitting the detection path in two spectral channels. To this end, the detection objective is followed by a 1x relay lens system (f_3 = f_4 = 100 mm, Thorlabs). A vertical slit is placed in the intermediate image plane with 400 µm horizontal size, which corresponds to half of the field of view. A dichroic filter at 505 nm (DMLP505, Thorlabs) creates two-colour replicas of the sample image, which are then formed on the detector through two band-pass filters (MF479-40 and MF535-22 emission filters, Thorlabs), two broadband mirrors (BBSQ1-E02, Thorlabs) and a tube lens (U-TLU-1-2, Olympus). These create the images of the CFP and the cpVenus fluorescent signals on the two sides of the CMOS sensor (Neo 5.5 sCMOS, 2560 × 2160 pixels, ANDOR). The laser power was set to 20 µW on the sample, which proved not to give relevant photobleaching during the experiment. To minimize the light dose on the sample, an automatic shutter opens the laser beam only when the camera is in acquisition mode. A white LED illuminator is used for trans-illumination, for sample alignment. The sample is held vertically in a custom-made 3D-printed chamber, filled with the imaging solution. The camera acquisition, sample translation stage and shutter are synchronized via a custom-made LabVIEW software. This software permits the observation of the two channels, to visualise their ratio in real time and to record the data. Camera binning was set to 1 x 1 and exposure times to 100 ms. Images were acquired every 5 s and at every time point a Z-stack of 30 planes spaced of 3 µm was acquired. Images were processed using FIJI by analyzing a single plane of the time series. To generate the images shown in *SI Appendix*, Figs. S2*A* and S4 the cpVenus/CFP calculated ratio (magenta) was superimposed to the first cpVenus emission image of the time series.

Root tip seedling LSFM Ca^{2+} imaging. Fluorinated ethylene propylene (FEP, Adtech FT2x3) tubes with an internal diameter of 0.8 mm and manually cut in 3 cm-long pieces using a razor blade, were cleaned first with 1 M NaOH, then with a diluted NaOH solution (0.5 M) and finally with 70% of ethanol (18). After washing with 1 M NaOH, a 10 min sonication was performed at each cleaning step. The tubes were then rinsed with MilliQ water and coupled with the heads of 10 µl pipette tips (manually cut), placed into cleaned pipette tip boxes and afterwards autoclaved at 121 °C for 20 min. The FEP tubes were then filled with the MS/2 medium used for the seed germination but in this case jellified with 0.5% Phytagel™ (w/v) (Duchefa) instead of plant agar (3, 18, 19). The tubes were filled from the bottom of the tubes using a P200 micropipette. To prevent the evaporation of water from the Phytagel™-based medium the top of the tubes was covered with a plant agar-based-medium plug, thus creating a small cap. After solidification, a sterilized scalpel was used to remove the exceeding cap medium. After seedlings germination and fluorescence inspection with a stereo microscope, the fluorescent seeds were quickly moved from the plate to the top of the tubes to avoid root drying, using sterilized pliers and without clamping them. Seedlings were placed over the top of the tubes, so the plantlets could grow inside the filled tubes. The tubes were transferred to a tip box that was finally filled with MS/2 liquid medium without sucrose and sealed to avoid contamination. To mount the tubes with the plant in the imaging chamber, we used a custom-made holder (3, 18) consisting of a hollow aluminium tube in which a pipette tip can be attached. The seedlings were let grow until the root tip emerged from the FEP tubes (7/8-day-old). When plants were ready to be imaged, we plugged the pipette tip with the tube into the hollow tube, and quickly moved the whole holder to the imaging chamber of the LSFM setup filled with imaging solution (5

mM KCl, 10 mM MES, 10 mM $CaCl_2$ pH 5.8 adjusted with TRIS), fixing it on a rotation and translation stage for the sample positioning. This procedure prevents any kind of damage or major stress to the root and maintains the seedling vertical. For the analysis of spatiotemporal dynamics of the [Ca^{2+}] variation, a volume of 120 µL (100X) for each tested amino acid was directly added to one corner of the imaging chamber (filled with 12 mL of imaging solution). The final concentration of the stimuli was 1 mM. The ratio images are representative of n = 3 experiments.

Quantitative imaging analysis. Fluorescence intensity was determined over regions of interest (ROIs), which corresponded to the meristematic cells of the root tip. cpVenus and CFP emissions were used for the ratio (R) calculations (cpVenus/CFP) and, where suitable, normalized to the initial ratio (R_0) and plotted versus time ($\Delta R/R_0$). For wide-field imaging background subtraction was performed independently for both channels before calculating the ratio. Kymograph was generated with the FIJI plugin using the yellow line reported in *SI Appendix*, Fig. S2*A*.

Yeast growth complementation assay. *Saccharomyces cerevisiae* strain K667 (vcx1/Δ, cnb1::LEU2, pmc1::TRP1) (12) was transformed with pYES2-URA empty vector (Invitrogen) or pYES2-URA harboring the *GLR3.3* coding sequence (10) in the BamHI/EcoRI sites. The same vector harboring the *Arabidopsis CCX2* (cation/Ca^{2+} exchanger 2) (14) was used as positive control. Transformants were selected for uracil prototrophy as reported in (20). For complementation studies, single URA-plus colonies were grown in SC-URA medium containing 2% (w/v) glucose (SD), pelleted, washed twice with sterile water and diluted to an OD_{600} of 0.1. Three µl of a 10-fold dilution were spotted onto SC-URA plates containing 2% (w/v) galactose (SG) supplemented with 1, 300 or 500 mM $CaCl_2$ and incubated at 30 °C for 3-5 days. All media were supplemented with 50 mM succinic acid/Tris (pH 5.5), 0.7% (w/v) yeast nitrogen base without ammonium sulfate, to prevent precipitation of Ca^{2+}, and 5 g/L NH_4Cl.

Cloning of the GLR3.3 LBD construct. The DNA portions codifying for *At*GLR3.3 S1 (residues 463-570) and S2 (residues 681-813) segments were amplified, joined by overlapping PCR (with the concomitant introduction of a Gly-Gly-Thr interspacing linker) and cloned into a pETM-14 vector (EMBL, Heidelberg, Germany) to produce an N-terminally histidine-tagged construct for expression in *E. coli*. Although a 2-residue linker is regularly reported in the literature for LBD constructs, a 3-residue Gly-Gly-Thr linker was designed because expected to be better accommodated in the crystal packing, in the light of *in silico* predictions of *At*GLR3.3 LBD secondary structure and careful alignment of the *At*GLR3.3 sequence with sequences from deposited LBD structures (using *Jalview*) (21).

Production and purification of the native protein (GLR3.3 LBD). Rosetta strain *E. coli* cells (Novagen, Merck Biosciences) were transformed with the above described pETM-14: *At*GLR3.3 LBD plasmid and grown at 37 °C in LB medium (supplemented with kanamycin and chloramphenicol) up to OD_{600} of 0.6-0.8. After cooling down the cultures at room temperature for 20 min, isopropyl β-D-1-thiogalactopyranoside (IPTG) was added to a final concentration of 0.1 mM and the growth continued at 20 °C for 16 h. The pelleted cells were resuspended in a buffer containing 50 mM TrisHCl pH 8.0, 500 mM NaCl, 15 mM imidazole, 2 mM β-mercaptoethanol, cOmplete™ EDTA-free protease inhibitor cocktail (Roche), 0.5 mM L-Glu or Gly. All buffers were supplemented with 0.5 mM L-Glu or Gly throughout purification to ensure stabilization of the construct. After sonication and centrifugation, the resulting supernatant was applied onto a nickel column (HisTrap FF, GE Healthcare). The imidazole-eluted sample was mixed with home-made His-tagged human rhinovirus 3C protease (protease:target protein molar ratio ≈ 1:600) and dialyzed overnight in a dialysis tube (SpectrumLabs, cutoff 4 kDa) to allow for tag cleavage and imidazole removal. The following day, a second passage through the nickel column was performed to separate the sample from both the tag and the protease and in the final size-exclusion chromatography column (Superdex200 10/300

GL, GE Healthcare) the 27kDa protein eluted as a symmetric peak compatible with either a monomer or a dimer (*SI Appendix*, Fig. S8*A*). A dynamic light scattering experiment showed that >99% of the protein in solution is monomeric (*SI Appendix*, Fig. S8*C*). Typical yields were of about 25 mg per liter of culture. The sample was monitored throughout purification by SDS-polyacrylamide gel electrophoresis and spectrophotometry. The final protein construct included 3 post-cleavage N-terminal residues (Gly-Pro-Met) immediately followed by Gly1 (see *SI Appendix*, Figs. S6 and S7 for construct sequence numbering) and was stored in the final size-exclusion chromatography buffer (10 mM HEPES pH 7.5, 150 mM NaCl, 0.5 mM EDTA, 0.5 mM L-Glu).

Production and purification of selenomethionine-substituted GLR3.3 LBD. Rosetta cells transformed with the same plasmid described above were grown in minimal M9 medium to OD_{600} of 0.3, supplemented with a cocktail of amino acids including L-selenomethionine, induced by 0.2 mM IPTG 15 min later and grown at 25 °C for 30 h, according to a metabolic inhibition protocol (22). Purification procedures were identical to the ones used for the native protein, except for the inclusion of 20 mM β-mercaptoethanol in all buffers. The incorporation of selenium was assessed on crystals right before data collection by analysis of the X-ray fluorescence emission spectra.

Dynamic light scattering. Measurement was performed on a Punk instrument (Unchained Labs) on GLR3.3 LBD + L-Glu at 1 mg/mL (37 µM) in 10 mM HEPES pH 7.5, 150 mM NaCl, 0.5 mM EDTA, 0.5 mM L-Glu, at 20 °C.

Dialysis to produce the apo protein. The final protein was expected to contain the amino acid ligand supplemented during purification (L-Glu or Gly) and for this reason was subjected to extensive dialysis against the storage buffer to force the complete release of the ligand (1:150 sample dilution in 8x 6h-passages, giving a final dilution of 10^{17}); the protein sample obtained was used in the binding assays. Turbidity of the sample and heavy precipitation reproducibly occurring after 3-4 dialysis steps strongly suggested a holo to apo transition; apo *At*GLR3.3 LBD was invariably more unstable than the holo (L-Glu or Gly) form, displaying lower solubility and shorter storage life.

Circular dichroism. Circular dichroism experiments were carried out on a J-810 spectropolarimeter (JASCO Corp.) equipped with a Peltier system for temperature control. All data were collected on 0.2 mg/mL (7 µM) protein solutions in 10 mM HEPES pH 7.5, 150 mM NaCl and 0.5 mM EDTA (± 0.5 mM L-Glu), placed in a cuvette with a path length of 0.1 cm. Spectra were recorded from 260 to 200 nm. Temperature ramps were monitored at 220 nm while temperature was increased from 20 to 95 °C at 1 °C/min. T_m was calculated as the first-derivative maximum of the temperature ramps.

Binding assays by microscale thermophoresis. The assays were performed on a Monolith NT.115 instrument (NanoTemper Technologies). To prepare the experiment, GLR3.3 LBD or GLR3.3 LBD S13A,Y14A in their apo form were conjugated to a fluorophore targeting surface lysines (Monolith Protein Labeling Kit RED-NHS, NanoTemper Technologies) and separated from the dye excess using desalting columns. The GLR3.3 LBD construct possesses 14 surface lysines, resulting in a satisfactory and reproducible conjugation process. Each curve was produced at 24 °C by the thermophoretic signal of 16 capillaries (MST power 40%) containing a fixed concentration of labelled protein (100 nM) and increasing concentrations of ligand, in 10 mM HEPES pH 7.5, 150 mM NaCl, 0.5 mM EDTA, 0.05% Tween20. All measurements recorded strong thermophoretic signals (response amplitudes between 4 and 15, signal to noise ratios between 8 and 13, in line with what is expected for unambiguous results with this technique), generating well-defined sigmoidal curves reaching plateau. For the control experiments in *SI Appendix*, Fig. S10, the fluorescent target (Cy5-labelled aptamer) specifically supplied by NanoTemper for the instrument was tested versus its ligand (AMP) and three of GLR3.3 amino acid ligands. All data were averaged and fit by the instrument software MO. Affinity Analysis (NanoTemper) according to the following formula:

$$F = U + \frac{(B-U)\cdot\left([ligand]+[protein]+K_d-\sqrt{([ligand]+[protein]+K_d)^2-4\cdot[ligand]\cdot[protein]}\right)}{2\cdot[protein]}$$

where F is the fraction of protein bound to the ligand, while U and B represent the response values (normalized fluorescence) of the unbound and bound states, respectively. A general review on this technique is available in (23), along with considerations about controls in (24). Successful application of this technique to LBDs of iGluRs is reported in the literature (25).

Crystallizations. Crystallization screens were performed on an Oryx robot (Douglas Instruments) by the sitting drop vapor diffusion method and manually refined by the hanging drop technique. GLR3.3 LBD (native or SeMet-substituted) purified in the presence of L-Glu or extensively dialyzed GLR3.3 LBD supplemented with 3 mM L-Cys or Gly or L-Met was mixed 2:1 at initial concentration of 12 mg/mL (445 µM) with commercial solutions (Hampton Research) in Greiner Bio-One plates and incubated at 20 °C. Hits showed up within 7 days. GLR3.3 LBD + L-Glu crystals were subsequently optimized to the final reservoir condition 100 mM sodium acetate pH 4.6, 240 mM ammonium sulfate, 30% (w/v) PEG monomethyl ether 2,000. For GLR3.3 LBD + Gly or L-Cys or L-Met, initial crystals were directly used for data collection and were obtained in the following conditions: (+ Gly) 100 mM sodium citrate tribasic pH 5.6, 2 M ammonium sulfate, 200 mM potassium sodium tartrate; (+ L-Cys or + L-Met) 100 mM HEPES pH 7.5, sodium citrate tribasic 1.4 M. SeMet-substituted GLR3.3 LBD gave crystals in 100 mM MES pH 6.5, 200 mM ammonium sulfate, 20% (w/v) PEG 8,000. All cryoprotectants were prepared by adding 25% (v/v) glycerol to the reservoir solution.

Data collections and structure solution. Statistics for data collection, phasing and refinement are summarized in *SI Appendix*, Table S1. For both the native GLR3.3 LBD + L-Glu and the SeMet GLR3.3 LBD + L-Glu datasets, diffraction data were collected at 100K on the ID29 beamline (26) at the European Synchrotron Radiation Facility, Grenoble (France) using the Pilatus 6M-F pixel detector (Dectris). The native data set was collected at a wavelength of 1.000 Å and initially indexed in space group C2 with a resolution of 2.0 Å; the anomalous data set was collected close to the Se *K*-edge at 0.979 Å and showed a tetragonal space group ($P4_32_12$) with a resolution of 2.4 Å. The datasets for GLR3.3 LBD + Gly, L-Cys and L-Met (all in the orthorhombic space group $P2_12_12_1$, with resolutions of 1.6 Å, 2.5 Å and 3.1 Å, respectively) were collected remotely at 100K at the Diamond Light Source (Didcot, UK) on the Eiger2 X 16M detector (Dectris) of beamline I04 at a wavelength of 0.9795Å. Several applications from the *CCP4* suite were used throughout processing (27) (*SI Appendix*, Table S1). Diffraction data were processed using *XDS* (28) and scaled and merged with *AIMLESS* (29); the high-resolution data cut-off was based on the statistical indicators $CC_{1/2}$ and CC* (30). Molecular replacement (MR) was initially attempted with no success on the native L-Glu dataset with standard software, using search models identified through *BLAST*, *PSI-BLAST* (31), *FFAS* (32) or rationally edited LBD models based on the large number of bacterial and eukaryotic GLR LBDs structures available from the Protein Data Bank; pruning of the solvent-exposed loops and sequential use of either of the two lobes of known LBDs were tested in MR, producing in some cases partial solutions that did not improve after subsequent manipulation. The observation that the *At*GLR3.3 LBD reflects the topological arrangement of known LBDs with a substantial displacement in the Cα trace (more pronounced in domain 2) provides a possible *a posteriori* explanation for these failures. Experimental phasing on the SeMet dataset was first attempted with various standard software with no success, at least in our hands. The phase problem was finally solved by MRSAD phasing (33, 34), by which approximate experimental phases, obtained by locating some of the selenium atoms and successively improved by density modification, allowed to build a partial model; phases extracted from this model were then combined with the initial anomalous phases to produce a more accurate set of phases and an improved electron density map, as described more in detail below. A highly fragmented and partially wrong model was firstly obtained by the *CRANK2* experimental phasing

pipeline (35, 36), using the SeMet dataset as both native and anomalous input: decreasing R-factor during the initial model building and refinement, as well as R_{free} < 0.50, good electron density for some parts of the structure and accordance between the position of some of the SeMet residues and the anomalous map led to consider the model as a partial, promising solution, albeit fragmented and incorrect in several parts. The model was then gradually improved by extensive model building with the *BUCCANEER* software (37) and the geometry of the model and the quality of the electron density map were improved with *BUSTER* (38, 39). Subsequent MRSAD-phasing in 'rebuild mode' in *CRANK2* (36) using the *BUSTER* model and the anomalous dataset improved the map; the number of substructure improvement iterations and the number of model building cycles were increased to 5 and 15, respectively (compared to the default *CRANK2* values); all expected SeMet in the model were in agreement with the map. Simulated annealing refinement by *phenix.refine* (40) was then used to improve the geometry and the obtained model was placed into the unit cell of the native data (L-Glu dataset) by MR with *MOLREP* (41). For the subsequent model building of the native L-Glu dataset, the P1 space group was chosen because of better data statistics compared to the alternative monoclinic C2 assignment, good overall completeness of the data and the presence of only two molecules in the unit cell. The model was refined against native data by iterative rounds of *REFMAC5* restrained refinement (42), *phenix.refine* and manual editing in *Coot* (43). During refinement, additional positive density observed in both cavities in the $2|\boldsymbol{F}|_o-|\boldsymbol{F}|_c$ and $|\boldsymbol{F}|_o-|\boldsymbol{F}|_c$ electron density maps allowed to unambiguously identify the L-Glu ligand (Fig. 2*B-E* and *SI Appendix*, Fig. S11*A-D*). Water molecules were added with *ARP/wARP* (Solvent module) (44) and the final stereochemistry was assessed by *MolProbity* (http://molprobity.biochem.duke.edu/) (45). MR by *MolRep* (41) using the ligand-deprived L-Glu structure allowed to obtain the Gly, L-Cys and L-Met structures. The presence of the ligands was confirmed by bias-reduced simulated-annealing OMIT maps generated through the *PHENIX* suite (40). All 14 individual chains from the four crystal structures display an excellent structural match in their Cα traces (max rmsd 0.55 Å); the only significant difference is confined to the C-terminal stretch Lys240-Thr244 (including Cys243, which forms a disulfide bridge with Cys179), whose density has two alternative traces in 4 out of 14 chains and is absent in the rest: however, in almost all cases the density for the disulfide bridge is detectable. For the L-Met dataset, a moderate degree of anisotropy was detected and therefore the reflection data were subjected to ellipsoidal truncation and anisotropic scaling through the UCLA Diffraction Anisotropy Server (http://services.mbi.ucla.edu/anisoscale/) (46); moreover, 29 residues in the chain B of the L-Met-bound structure (all comprised in domain 2) displayed missing or very poor density and therefore were not modelled.

Preparation of figures. All structural representations and superpositions were prepared with *PyMOL* (The PyMOL Molecular Graphics System, Version 1.3 Schrödinger, LLC).

Site-directed mutagenesis. All mutations listed in *SI Appendix*, Table S2 were obtained using QuikChange Site-Directed Mutagenesis Kit (Stratagene) on the above described pETM-14: *At*GLR3.3 LBD plasmid and sequence-verified.

Expression tests of GLR3.3 LBD mutants. Each of the plasmids bearing a mutant version of GLR3.3 LBD was transformed into Rosetta strain *E. coli* cells. Small-scale (10 mL) cultures were grown at 37 °C in LB medium (supplemented with kanamycin and chloramphenicol) up to OD_{600} of 0.6-0.8. After that, they were subjected to either expression condition 1 (induction by 1 mM IPTG followed by shaking at 37 °C for 3 h) or 2 (induction by 0.1 mM IPTG followed by shaking at 20 °C for 16 h). The pelleted cells were then subjected to a shortened small-scale purification protocol limited to sonication and centrifugation, and samples for SDS-PAGE analysis were taken. A wild-type version of GLR3.3 LBD was included in all tests as positive control.

Homology modelling. All models were generated using the online server SWISS-MODEL (swissmodel.expasy.org) (47) providing the GLR3.3 LBD + L-Glu structure as input. Final model quality was assessed by the *MolProbity* score and QMEAN Z-score included in SWISS-MODEL calculations (see *SI Appendix*, Table S3 for details). To generate the GLR3.3 LBD-based models, the following residues from separate S1 and S2 segments (interspaced with the GGT linker) were used: GLR1.2, residues 441-547, 655-776 (numbered 1-232 in Fig. 3*C*); GLR1.4, residues 445-555, 663-785 (numbered 1-237 in Fig. 3*D*); GLR3.1, residues 469-575, 686-808; GLR3.4, residues 493-597, 708-836 (numbered 1-237 in Fig. 3*B*); GLR3.5, residues 487-590, 701-828. For the UniProt KB accession numbers of *At*GLR isoforms, see 'Sequence alignments' in this Appendix.

Pocket volume calculations. The CASTp software (http://sts.bioe.uic.edu/castp/) (48) was used to calculate the Connolly's solvent-excluded volume of the binding pocket, corresponding to the volume of the cavity contained within the contact molecular surface. The calculations were performed on the two datasets with best resolution, producing similar results: 196 $Å^3$ for the GLR3.3 + L-Glu pocket and 189 $Å^3$ for the GLR3.3 + Gly pocket.

Sequence alignments. Protein sequence alignments were performed with ClustalOmega (https://www.ebi.ac.uk/Tools/msa/clustalo/) (49). However, all alignments were manually corrected after careful inspection of the superimposed structures. All final figures of alignments were prepared with ESPript (http://espript.ibcp.fr) (50). UniProtKB primary accession numbers (https://www.uniprot.org/) of all protein sequences used in the alignments are: *At*GLR1.1 Q9M8W7, *At*GLR1.2 Q9LV72, *At*GLR1.3 Q9FH75, *At*GLR1.4 Q8LGN1, *At*GLR2.1 O04660, *At*GLR2.2 Q9SHV1, *At*GLR2.3 Q9SHV2, *At*GLR2.4 O81776, *At*GLR2.5 Q9LFN5, *At*GLR2.6 Q9LFN8, *At*GLR2.7 Q8LGN0, *At*GLR2.8 Q9C5V5, *At*GLR2.9 O81078, *At*GLR3.1 Q7XJL2, *At*GLR3.2 Q93YT1, *At*GLR3.3 Q9C8E7, *At*GLR3.4 Q8GXJ4, *At*GLR3.5 Q9SW97, *At*GLR3.6 Q84W41, *At*GLR3.7 Q9SDQ4; *Dm*GluR1A Q03445; *Av*GluR1 E9P5T5; *Rn*GluA2 P19491; *Hs*GluK1 P39086; *Hs*GluN2A Q12879; *Ec*GlnBP P0AEQ3; *Ss*GluR0 P73797; *Os*GLR3.1 Q7XP59. Of those sequences for which a UniProtKB record is not available, the entry in the NCBI Protein database (https://www.ncbi.nlm.nih.gov/protein) is: *Pp*GLR1 XP_024390787.1; *Br*GLR3.4 XP_009118614.1. For Gin_bil2 (*Ginkgo biloba* putative GLR2) the sequence of isoform 8 (locus 13956) is taken from (51).

Statistical analysis. All the data are representative of at least ≥ 3 experiments. Reported traces are averages of traces from all single experiments used for the statistical analyses. Results are reported as averages ± standard deviations (SD). Statistical significance was assayed by Student t test and validated using One-way ANOVA (ANalysis Of VAriance) and post-hoc Tukey HSD (Honestly Significant Difference) tests.

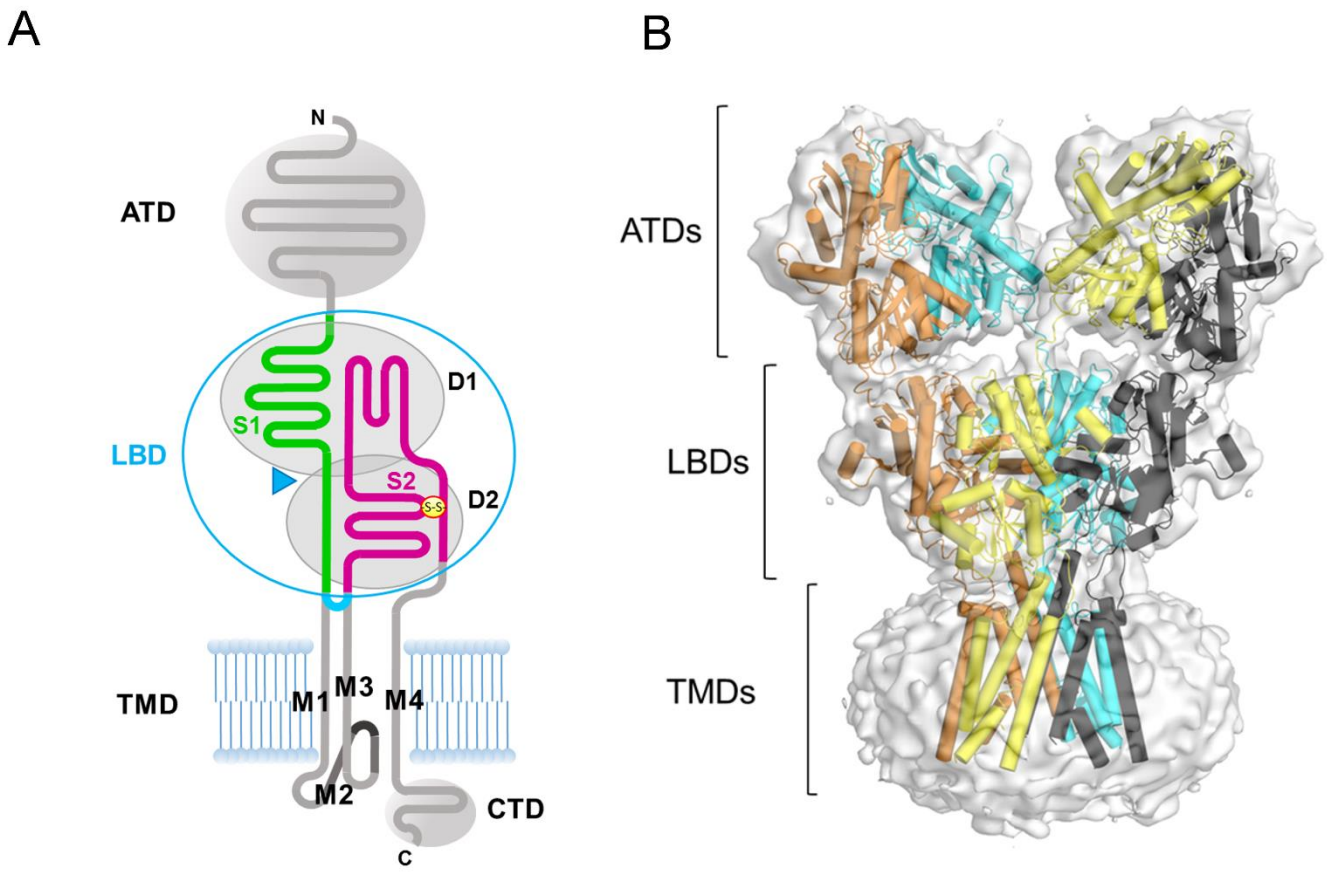

Fig. S1. Structure of iGluR/GLR channels. (*A*) General representation of one eukaryotic iGluR/GLR subunit. The functional channel is a homo- or heterotetramer of this subunit. Segment S1 is represented in green, S2 in magenta. The bilobed ligand-binding domain (LBD) is made up of domains 1 and 2 (D1 and D2); D1 residues are mainly contributed by segment S1 and D2 residues are mainly contributed by segment S2. The ligand (blue triangle) sits in a cleft between D1 and D2. The blue boundary encloses the *At*GLR3.3 LBD construct described in this work, with an arch indicating the site of the linker junction. The disulfide bridge (mostly conserved in eukaryotes) ties the final stretch of S2 to the D2 core. ATD, aminoterminal domain; M1 to M4: transmembrane segments of the transmembrane domain (TMD); CTD, C-terminal domain. (*B*) View of homotetrameric GluA2 (rat AMPA-subtype iGluR; PDB ID 5kbv, EMD ID 8232) (52). The 6.8-Å resolution cryo-EM map is shown as transparent surface and the four subunits of the model are shown in different colors with cylinder representation of α-helices. *A* is the general scheme of each one of these four subunits. Figure produced with *PyMOL* (The PyMOL Molecular Graphics System, Version 1.3 Schrödinger, LLC) from publicly available data.

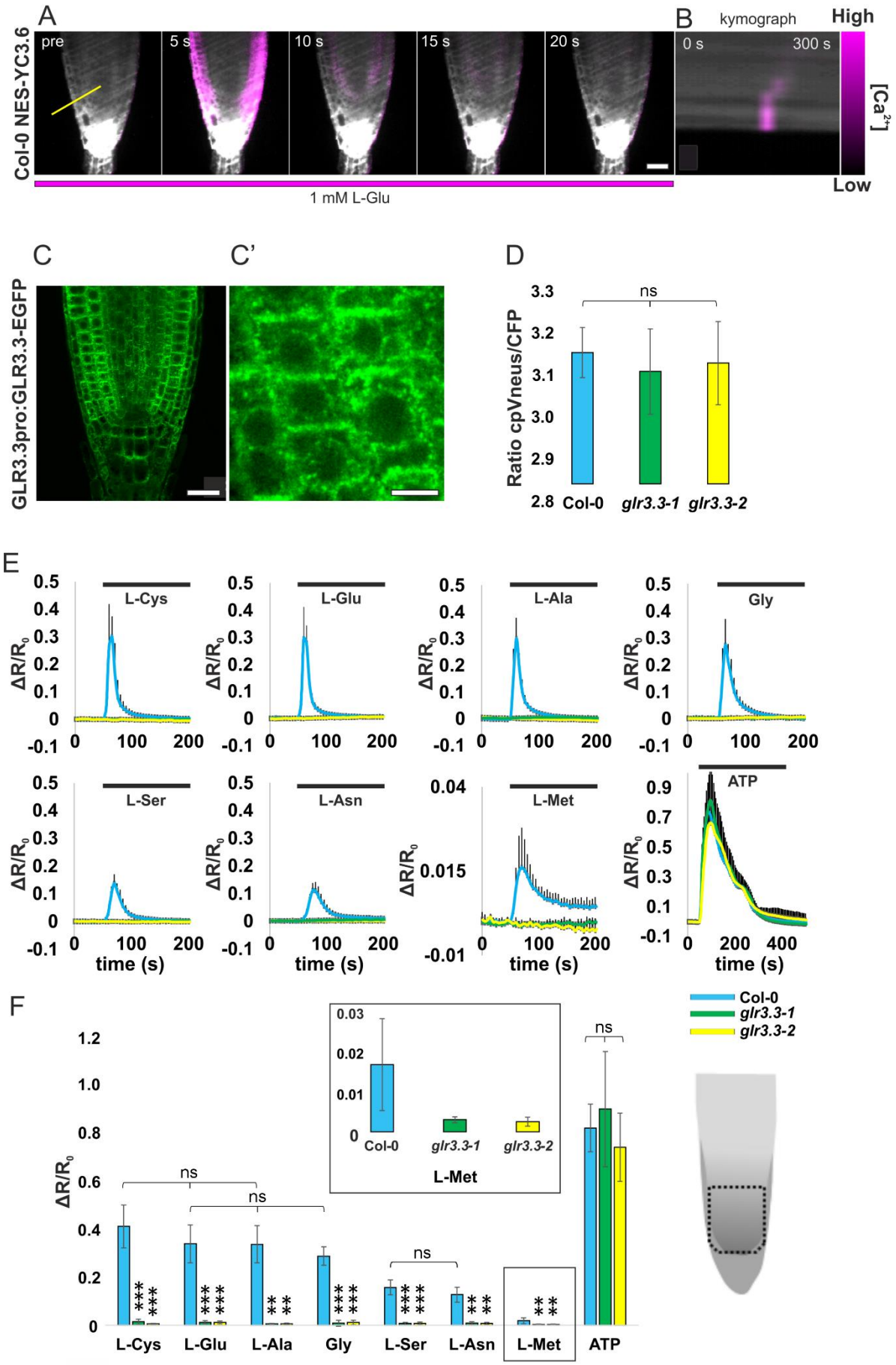
A
Col-0 NES-YC3.6
pre
5 s
10 s
15 s
20 s
1 mM L-Glu
B
kymograph
High
0 s
300 s
[Ca2+]
Low
C
C'
GLR3.3pro:GLR3.3-EGFP
D
Ratio cpVneus/CFP
ns
Col-0
glr3.3-1
glr3.3-2
E
L-Cys
L-Glu
L-Ala
Gly
L-Ser
L-Asn
L-Met
ATP
ΔR/R0
time (s)
F
Col-0
glr3.3-1
glr3.3-2
ns
L-Met
L-Cys
L-Glu
L-Ala
Gly
L-Ser
L-Asn
L-Met
ATP

373

(previous page)

Fig. S2. Amino acid-induced $[Ca^{2+}]_{cyt}$ increase in *A. thaliana* root tip cells depends on GLR3.3 activity. (*A*) Ratiometric purple-color images superimposed to cpVenus images from a representative time series of *Arabidopsis* Col-0 root tips expressing NES-YC3.6 treated with 1 mM of L-Glu visualized by LSFM. The number in each image indicates the time passed after acquisition start in seconds. Scale bar = 25 µm. (*B*) Kymograph analysis (performed on the yellow line of 1 pixel-width) showing the progression of the L-Glu-induced $[Ca^{2+}]_{cyt}$ increase with signal percolation from lateral root cells to the stele. (*C*) Confocal image of a representative root tip meristem of an *Arabidopsis* seedling expressing the GLR3.3-GFP (green color in the image) chimeric protein driven by the GLR3.3 promoter. Scale bar = 25 µm. (*C'*) Magnification of root meristem cells shown in *C*. Scale bar = 5 µm. (*D*) Steady state cpVenus/CFP ratios of the Region Of Interest (ROI) (corresponding to the area indicated within the black dashed line in the schematic drawing at the right bottom of the figure) in root tip cells imaged under continuous perfusion preceding (averaged over 50 sec time window) amino acid treatments of Col-0 (light blue), *glr3.3-1* (green) and *glr3.3-2* (yellow) knock out alleles; n ≥ 8; ns: not statistically significant. (*E*) Root tips of seedlings expressing NES-YC3.6 in Col-0, *glr3.3-1* and *glr3.3-2* imaged as in *D* treated with 1 mM of L-Cys, L-Glu, L-Ala, Gly, L-Ser, L-Asn, L-Met and 0.1 mM of external ATP. The same ROI as in *D* in the root tip meristematic zone was analyzed and plotted over time for the averaged cpVenus/CFP ratio ± SD. The black line above the graphs indicates the amino acid or ATP exposure. (*F*) Maximal relative amplitude of cpVenus/CFP ratio as $\Delta R/R_0$ increase triggered by amino acids and ATP administration in the three analyzed genotypes. Inset: magnification of 1mM L-Met maximum response; n ≥ 4; error bars ± SD; ** $p<0.005$, *** $p<0.0005$; (Student t test); ns: not statistically significant; SD = standard deviation.

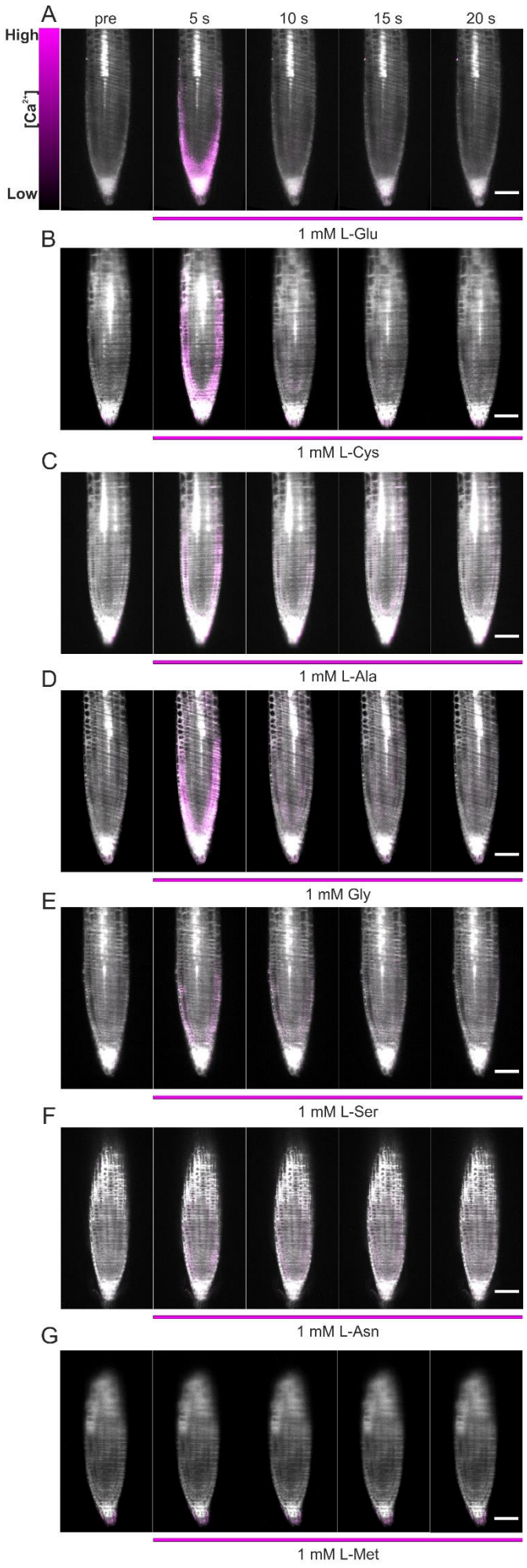

Fig. S3. Ratiometric purple-color images superimposed to cpVenus images from a representative time series visualized by LSFM of *Arabidopsis* Col-0 root tips expressing NES-YC3.6 treated with the 7 different amino acids used for the experiments shown in *SI Appendix*, Fig. S2*E*. The different time series show cpVenus/CFP ratio changes in response to 1 mM L-Glu (*A*), 1 mM L-Cys (*B*), 1 mM L-Ala (*C*), 1 mM Gly (*D*), 1 mM L-Ser (*E*), 1 mM L-Asn (*F*), 1 mM L-Met (*G*). Numbers in the images indicate the time passed after acquisition start in seconds. Scale bar = 55 µm; n = 3.

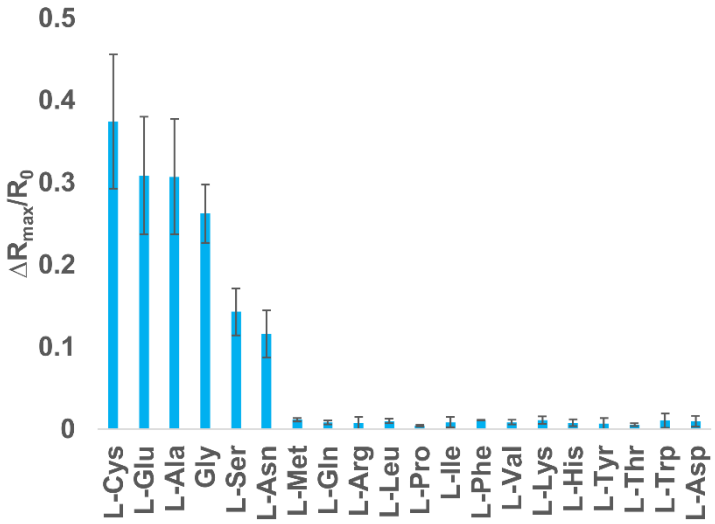

Fig. S4. Maximal relative amplitude of cpVenus/CFP ratio as $\Delta R/R_0$ increase triggered by the 20 amino acid L-enantiomers (1 mM) in the Col-0 wild-type seedling root tip expressing the NES-YC3.6 calcium sensor.

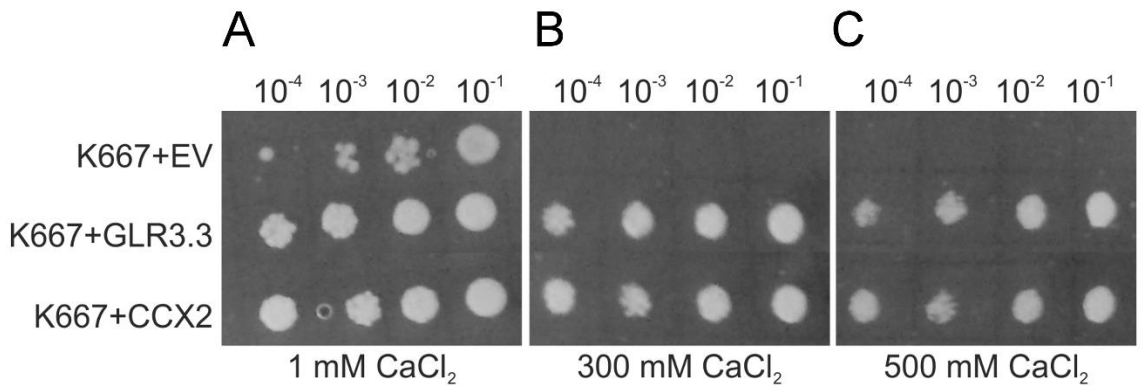

Fig. S5. Growth complementation assay of *S. cerevisiae* K667 transformed with pYES2-URA empty vector (EV), pYES2-URA harboring GLR3.3 or the *Arabidopsis* cation/Ca^{2+} exchanger CCX2 as positive control (14). Yeast cells were grown to OD_{600} of at least 1 and then 3 µl of serial dilutions were spotted onto SG-URA plates supplemented with 1 mM (*A*, control plate), 300 mM or 500 mM $CaCl_2$ (*B* and *C*, selective plates). The experiment is representative of two independent biological replicates showing similar results.

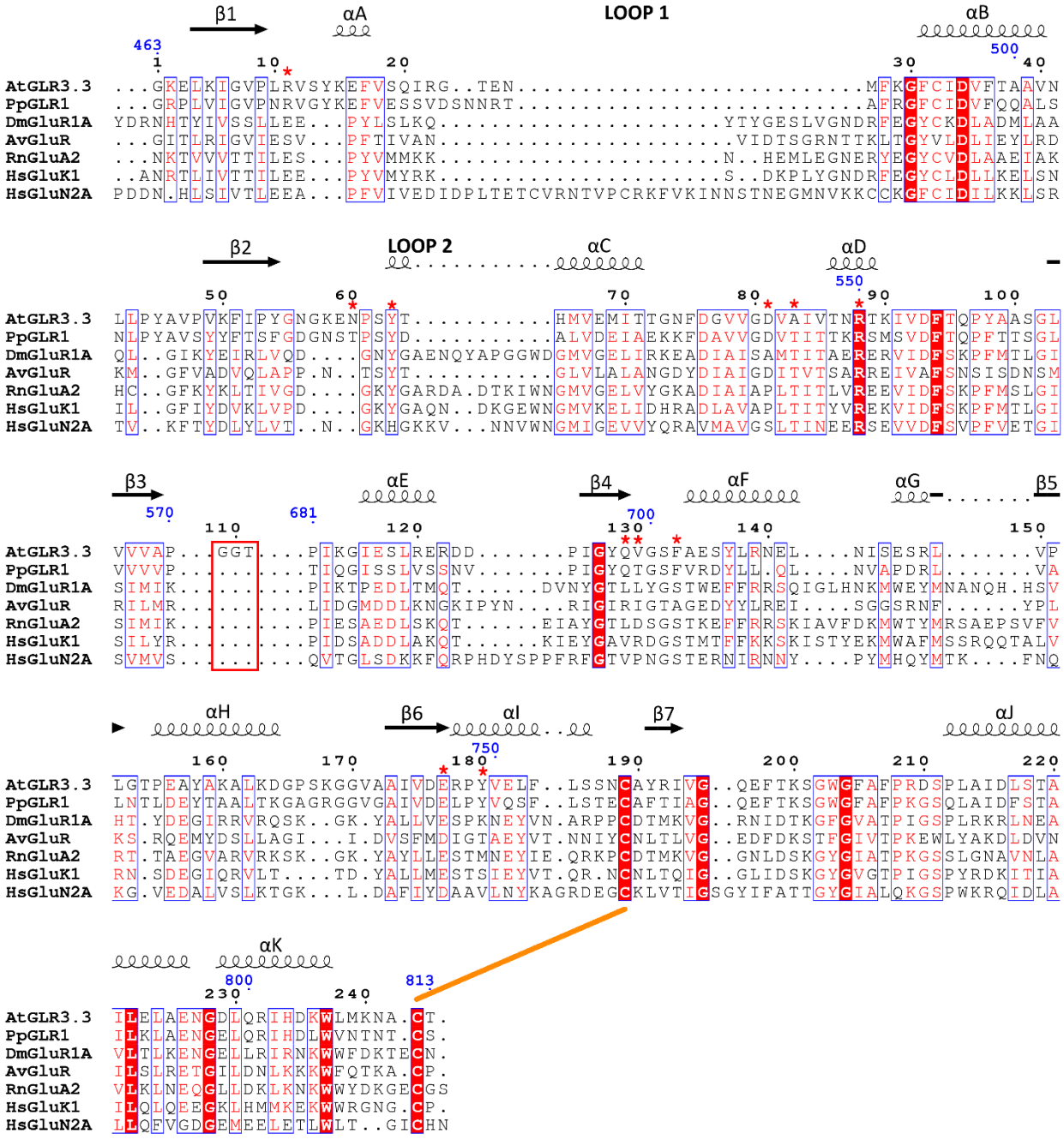

Fig. S6. Structure-based sequence alignment of LBDs (S1+S2 segments) from L-Glu-binding iGluRs/GLRs of different species. *At*GLR3.3: *Arabidopsis thaliana* GLR3.3 (this work); *Pp*GLR1: moss *Physcomitrella patens* GLR1; *Dm*GluR1A: *Drosophila melanogaster* GluR1A (PDB ID 5dt6); *Av*GluR1: rotifer *Adineta vaga* GluR1 (4io2); *Rn*GluA2: *Rattus norvegicus* AMPA-subtype GluA2 (1ftj); *Hs*GluK1: *Homo sapiens* kainate-subtype GluK1 (2zns); *Hs*GluN2A: *Homo sapiens* NMDA-subtype GluN2A (5h8f_A). At the top of the alignment, the *At*GLR3.3 secondary structure (α-helices as coils, β-strands as arrows), full-length numbering (blue) and numbering of the construct used in this paper (black) are shown. Location of the intervening M1-M2-M3 sequence (replaced by the GGT linker in the *At*GLR3.3 construct of this work) is indicated by a red box. The two Cys residues forming the disulfide bridge are connected by an orange line. Residues involved in ligand binding in the *At*GLR3.3 LBD structure are marked with red stars. See *SI Appendix*, Materials and Methods for the production of this alignment.

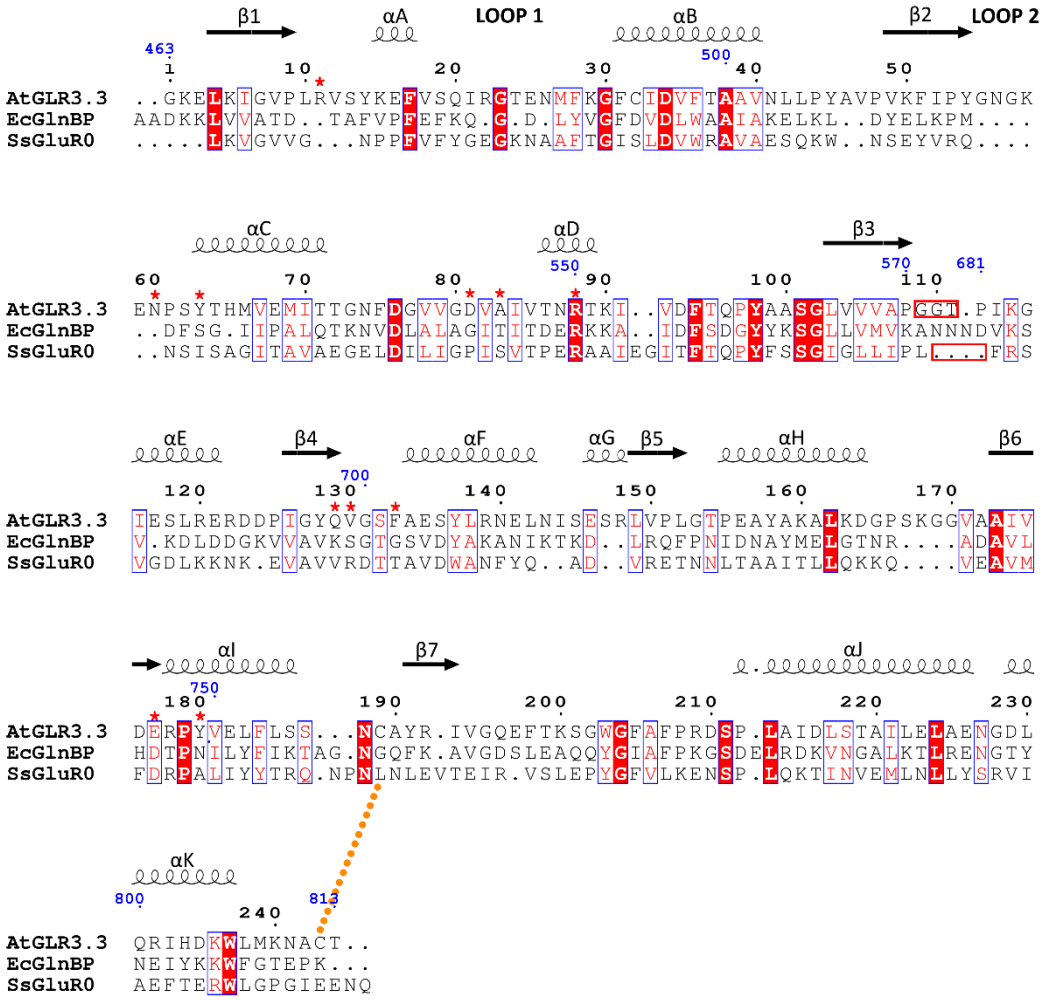

Fig. S7. Structure-based sequence alignment of LBDs (S1+S2 segments) of *At*GLR3.3 with prokaryotic homologous proteins. *Ec*GlnBP: *Escherichia coli* glutamine-binding protein (PDB ID 1wdn); *Ss*GluR0: cyanobacterium *Synechocystis sp.* GluR0 (1ii5). At the top of the alignment, the *At*GLR3.3 secondary structure (α-helices as coils, β-strands as arrows), full-length numbering (blue) and numbering of the construct used in this paper (black) are shown. Location of the intervening M1-M2-M3 sequence (replaced by the GGT linker in the *At*GLR3.3 construct of this work) is indicated by red boxes. Note that *Ss*GluR0 possesses transmembrane segments like *At*GLR3.3, whereas *Ec*GlnBP is a soluble clamshell-shaped periplasmic protein. The position of the disulfide bond in *At*GLR3.3 is indicated by orange dots. Residues involved in ligand binding in the *At*GLR3.3 LBD structure are marked with red stars. See *SI Appendix*, Materials and Methods for the production of this alignment.

A

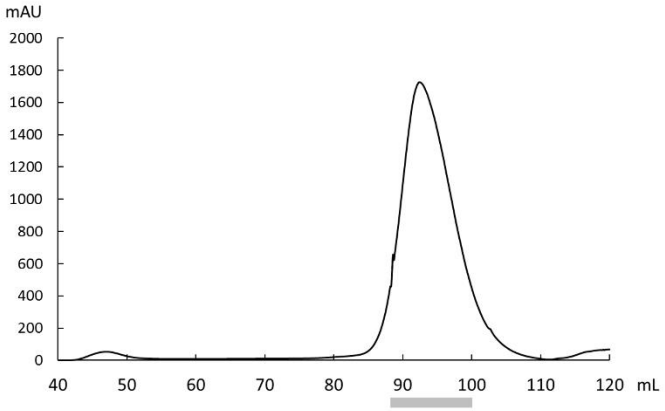

B

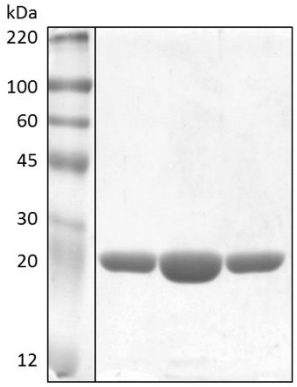

C

GLR3.3

Date:	10/13/2017 11:14:43 AM	**Temperature:**	19.94°C	**Data Filter:**	Default
Solvent:	PBS	**Solute:**	-	**Laser:**	100 %
Intensity:	674,314 counts/s	**Intercept:**	0.56	**Attenuator:**	75 %
Z - Av. Diameter:	23.46nm	**Std. Deviation:**	0.01nm	**MW model:**	Globular Proteins
Polydispersity:	0.06 %	**Pd. Index:**	0.000	**Remark:**	-

Peak #	Mean Dh (nm)	Mode Dh (nm)	Std. Dev. (nm)	Polydisp. (%)	Est. MW. (kDa)	Intensity (%)	Mass (%)	Volume (%)	Number (%)
1	4.09	4.87	1.78	43.52	25.28	39.52	99.89	99.97	100.00
2	77.45	87.67	31.89	41.18	Out of Range	60.48	0.11	0.03	0.00

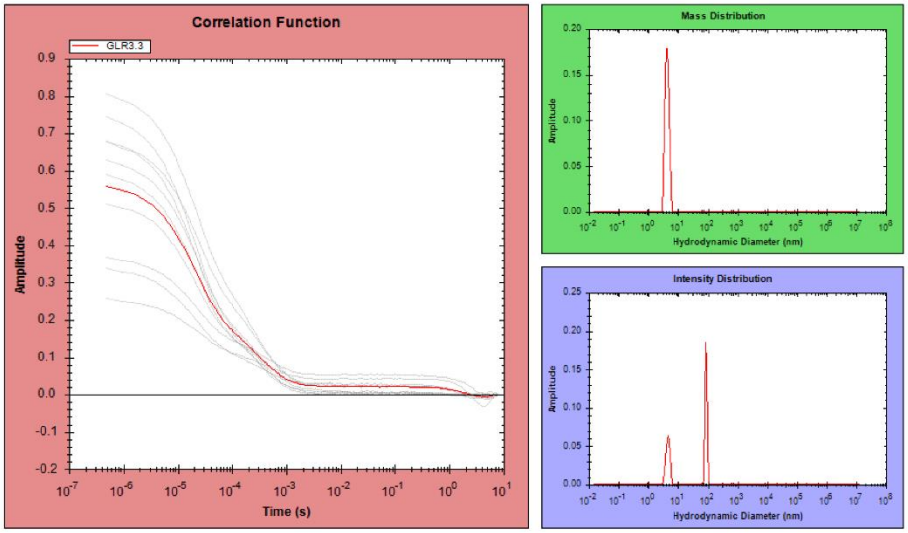

D

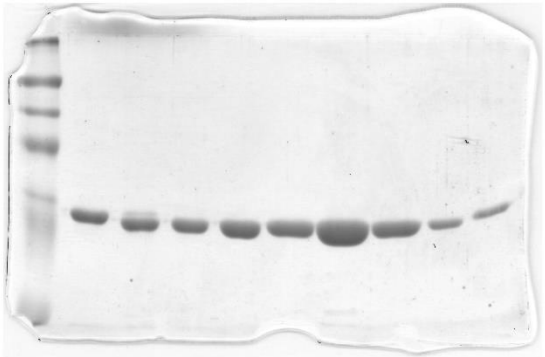

456

(previous page)

Fig. S8. Purification and characterization of GLR3.3 LBD. (*A*) Elution profile of GLR3.3 LBD from a preparative size-exclusion chromatography column (Superdex200 16/60, GE Healthcare) equilibrated with 10 mM HEPES pH 7.5, 150 mM NaCl, 0.5 mM EDTA, 0.5 mM L-Glu. The central fractions of the peak (marked) represent the final sample. (*B*) SDS polyacrylamide gel electrophoresis of three fractions (eluted from *A*) of purified GLR3.3 LBD (final sample), molecular weight ≈ 27kDa. Molecular weight marker: Blue Prestained Protein Standard, Broad Range (New England Biolabs). Gel: ExpressPlus PAGE (GenScript). (*C*) Report from a dynamic light scattering experiment on purified GLR3.3 LBD (1 mg/mL) loaded with L-Glu. The estimated molecular weight (25.28 kDa) is in agreement with the expected one for a monomeric sample (26.92 kDa). Instrument: Punk (Unchained Labs). (*D*) Original scan used to prepare the image in *B*.

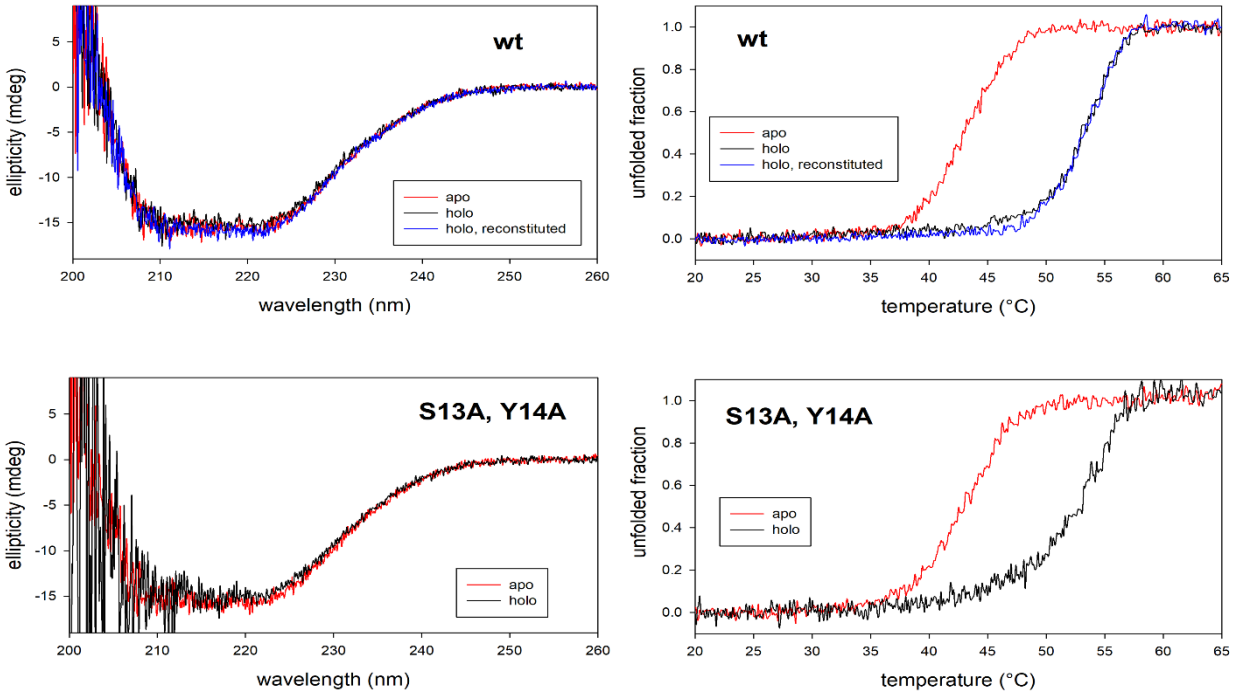

Fig. S9. Circular dichroism characterization of GLR3.3 LBD (wt, top, and mutant S13A-Y14A, bottom). Left panels: far-UV CD spectra; right panels: temperature ramps (the change in ellipticity at 220 nm was normalized as unfolded fraction). Black traces: holo (L-Glu-loaded); red traces: apo; blue traces: reconstituted holo (the reconstituted holo was obtained by addition of L-Glu to the apo). T_m values from the wt GLR3.3 LBD temperature ramps are 53.7 °C (holo), 42.9 °C (apo) and 53.8 °C (reconstituted holo), whereas T_m values for GLR3.3 LBD S13A-Y14A are 53.7 °C (holo) and 43.2 °C (apo).

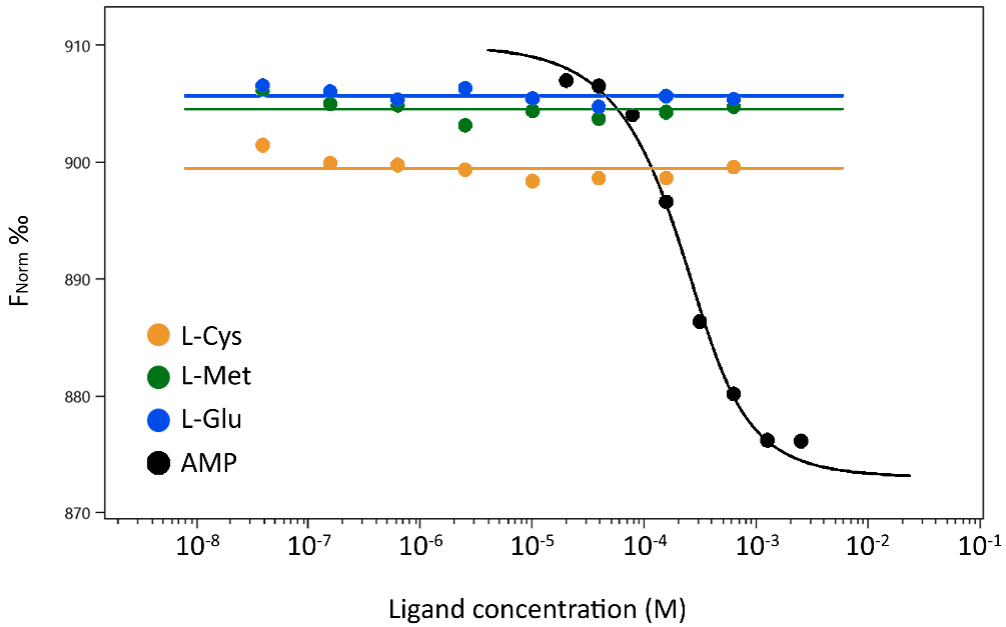

Fig.S10. Microscale thermophoresis control experiments. Cy5-labelled aptamer (reference fluorescent target) does not show the binding of L-Cys, L-Met, L-Glu at any concentration tested whereas the same reference efficiently binds AMP. The graph reports the concentration of the ligand in the logarithmic scale vs the thermophoretic signal expressed as normalized fluorescence (‰). Fitting of the binding curve of AMP, based on the equation reported in *SI Appendix*, Materials and Methods, produces a dissociation constant (K_d) of around 100 µM, as reported by the instrument data sheet provided by the manufacturer; horizontal lines interpolate the data for the non-binding compounds.

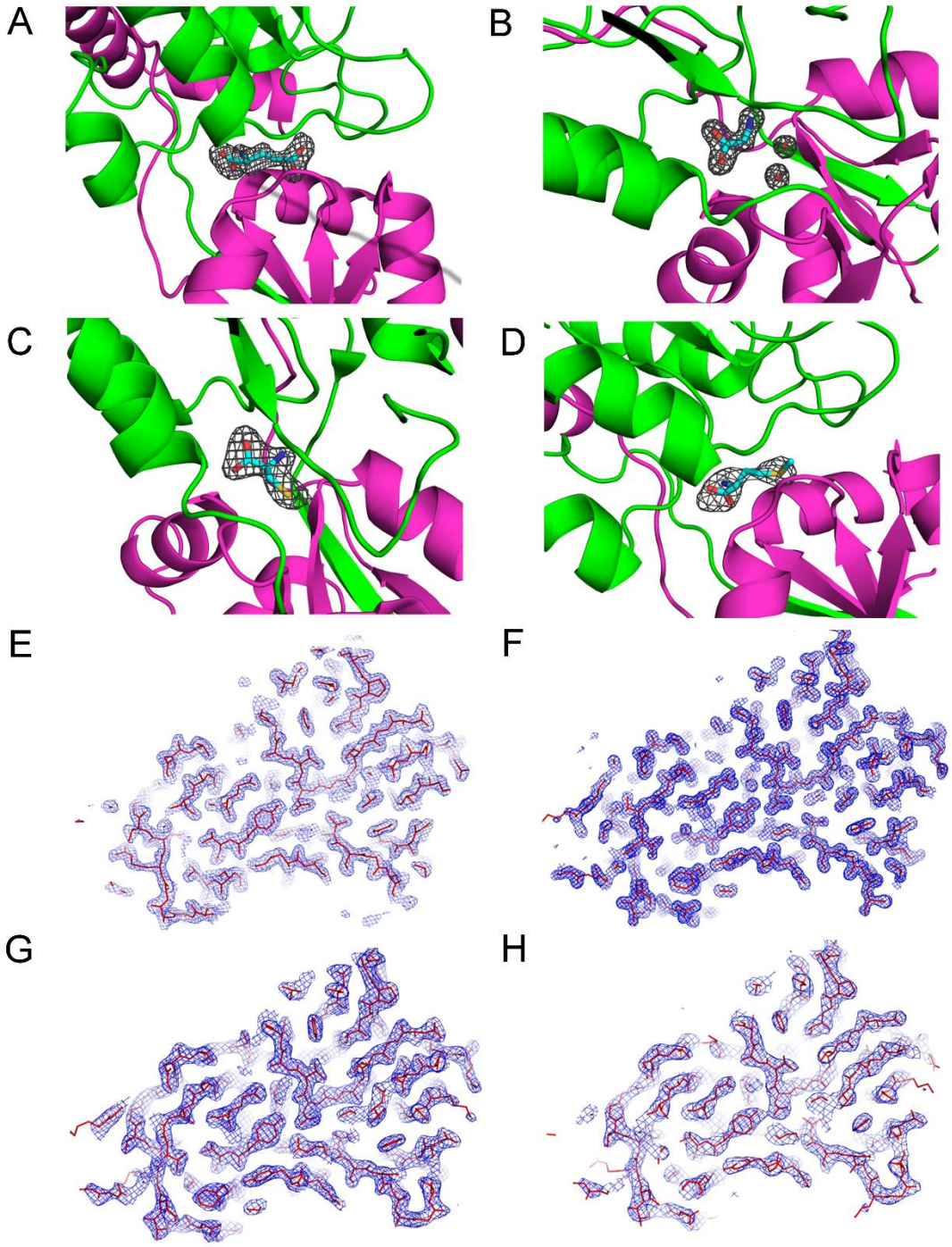

Fig. S11. Quality of the electron density maps. (*A-D*) The I***F***I$_o$-I***F***I$_c$ electron density omit maps contoured at 3.0 σ are shown for L-Glu (*A*), Gly and the two associated waters (*B*), L-Cys (*C*) and L-Met (*D*). In the early rounds of refinement protein models lacking any ligand molecule produced maps with clear I***F***I$_o$-I***F***I$_c$ electron densities for the ligands in the binding sites. The ligand molecules were then added in the following rounds of refinement. The color code is the same used in Fig. 2*A-E*. See Fig. 2*B-E* for the 2I***F***I$_o$-I***F***I$_c$ omit maps of the ligands. (*E-H*) Representative 2I***F***I$_o$-I***F***I$_c$ electron density maps contoured at 1.5 σ at the end of refinements for the L-Glu- (*E*), Gly- (*F*), L-Cys- (*G*) and L-Met- (*H*) containing datasets.

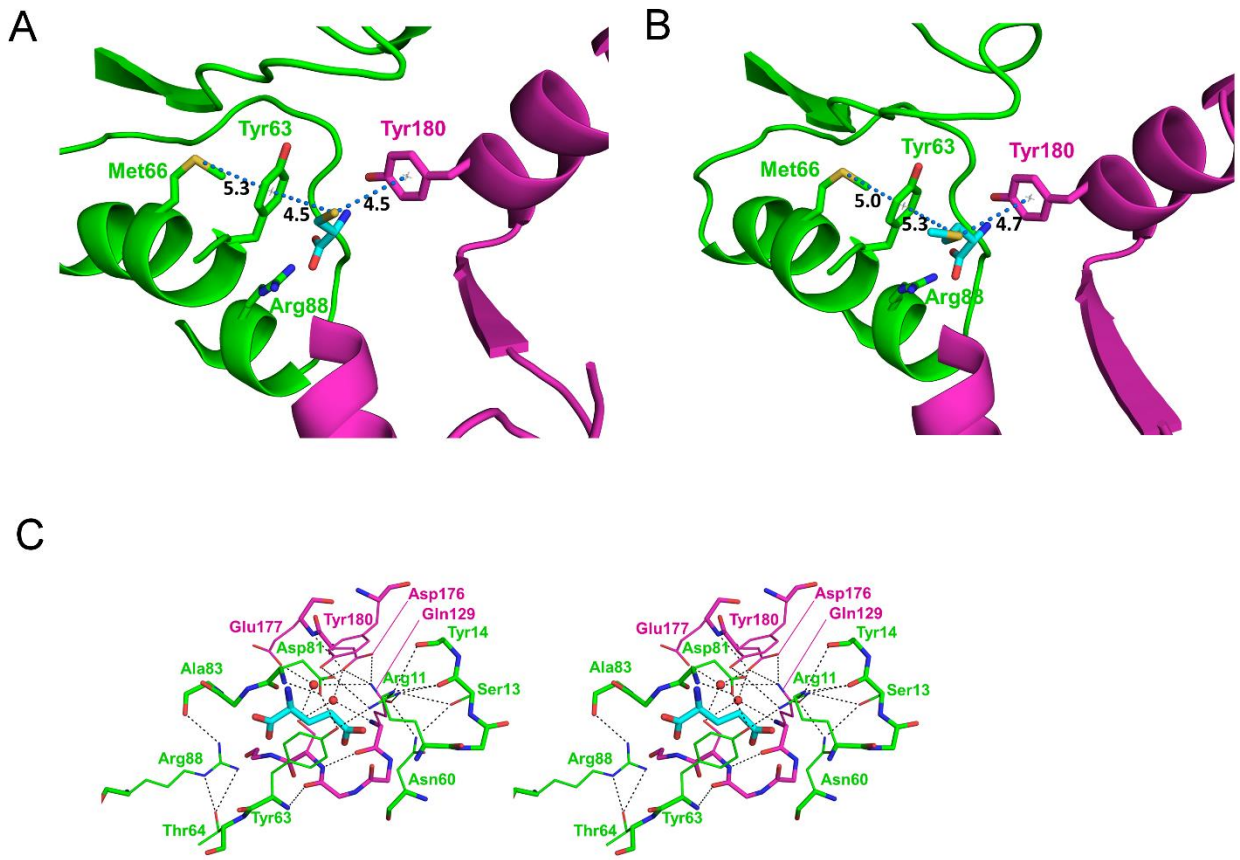

Fig. S12. Structural details of selected binding pockets in GLR3.3 LBD structures. (*A*-*B*) Close-up view of the ligand binding pocket in the crystal structures of GLR3.3 LBD + L-Cys (*A*) and L-Met (*B*). The ligands (cyan) and relevant side chains are in stick representation. Protein atoms from the S1 segment are green, from the S2 segment magenta. Oxygen is red, nitrogen blue, sulfur yellow. The orientation highlights the series of sulfur/π interactions (blue dashes) generated by the presence of the L-Cys and L-Met ligands. An almost straight line connects Met66 sulfur, the center of Tyr63 ring and the ligand sulfur. Distances between sulfur atoms and centers of the aromatic rings are indicated in Å. (*C*) View of the surroundings of the ligand-binding pocket of GLR3.3 LBD + L-Glu, with the same color codes as in *A*-*B*, showing the intricate network of interactions immediately outside the residues of Fig. 2*B*. Hydrogen or ionic bonds are shown as dashes; the ligand interactions shown in Fig. 2*B* have been omitted for clarity.

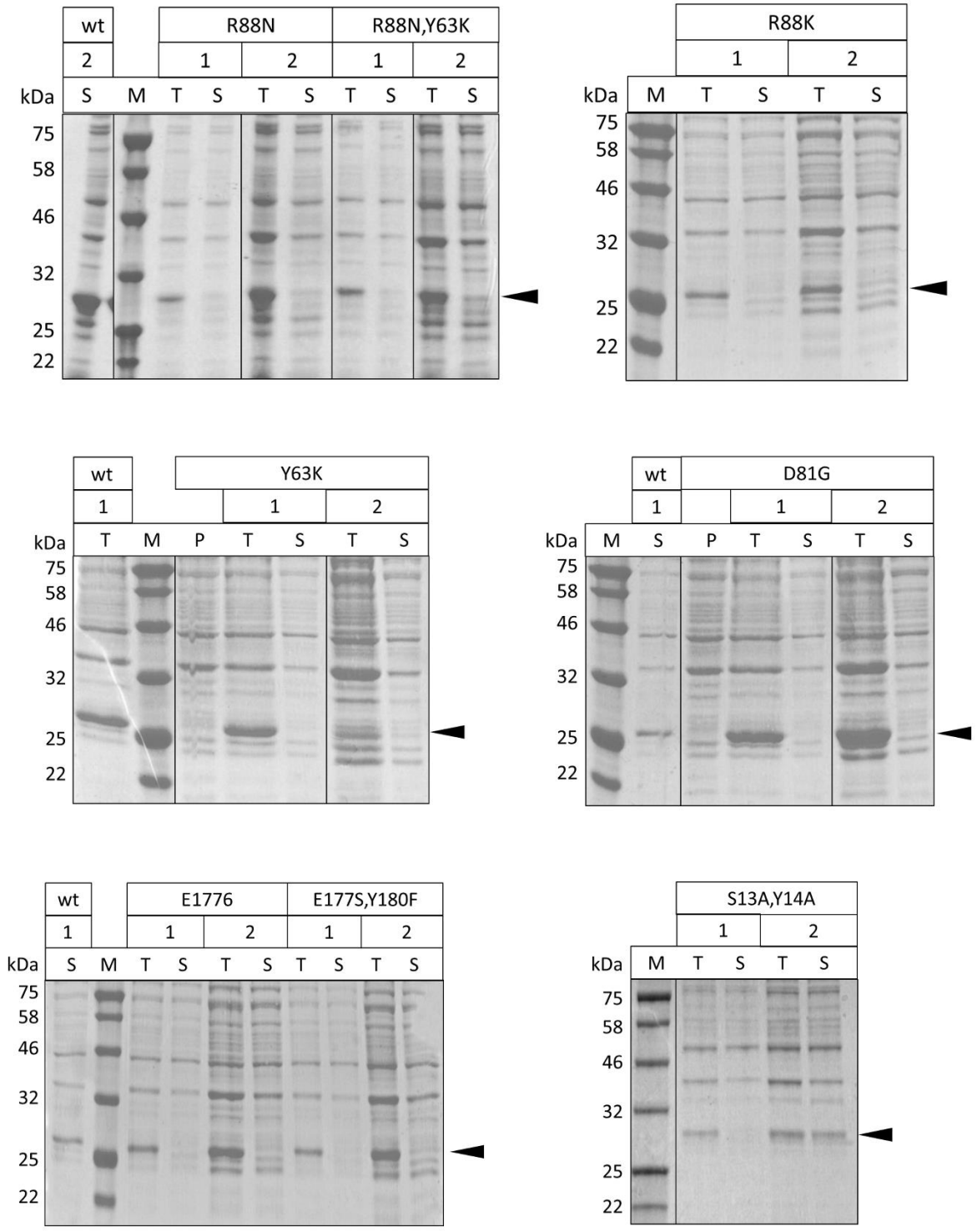

Fig. S13. SDS-polyacrylamide gel electrophoresis of fractions from small-scale expression tests of the GLR3.3 LBD mutants in *E. coli*. 1/2: condition 1 (induction by 1 mM IPTG followed by shaking at 37 °C for 3 h) or 2 (induction by 0.1 mM IPTG followed by shaking at 20 °C for 16 h); T: total cell lysate; S: soluble fraction; P: pre-induction sample; M: Blue Prestained Protein Standard, Broad Range molecular weight marker (New England Biolabs). Wt samples are included for comparison; His-tagged wt and mutant constructs have an approximate molecular weight of 29 kDa.

A

PROTEIN	K_d (μM)	*n*
3.3 LBD wt	2.2 ±0.5	5
3.3 LBD S13A-Y14A	2.1 ±0.4	2

B

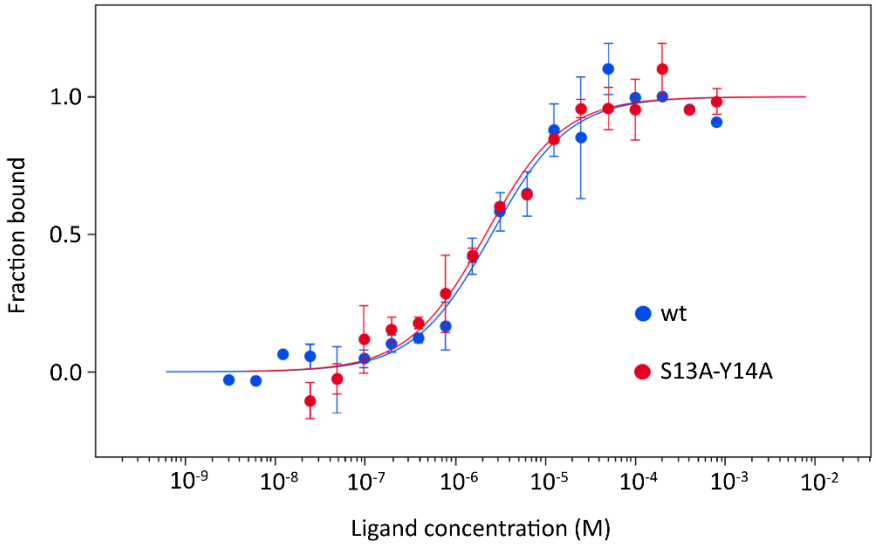

Fig.S14. Characterization of the binding properties of GLR3.3 LBD S13A-Y14A. (*A*) Values of the dissociation constant (K_d) ± SD for the binding of L-Glu to GLR3.3 LBD wt and S13A-Y14A, as determined by microscale thermophoresis; the values reported are averages from *n* repeats. (*B*) Fitting of the binding curves of L-Glu to GLR3.3 LBD wt and S13A-Y14A from the microscale thermophoresis experiments, based on the equation reported in *SI Appendix*, Materials and Methods; the graph reports the concentration of the ligand in logarithmic scale vs the thermophoretic signal normalized as fraction bound.

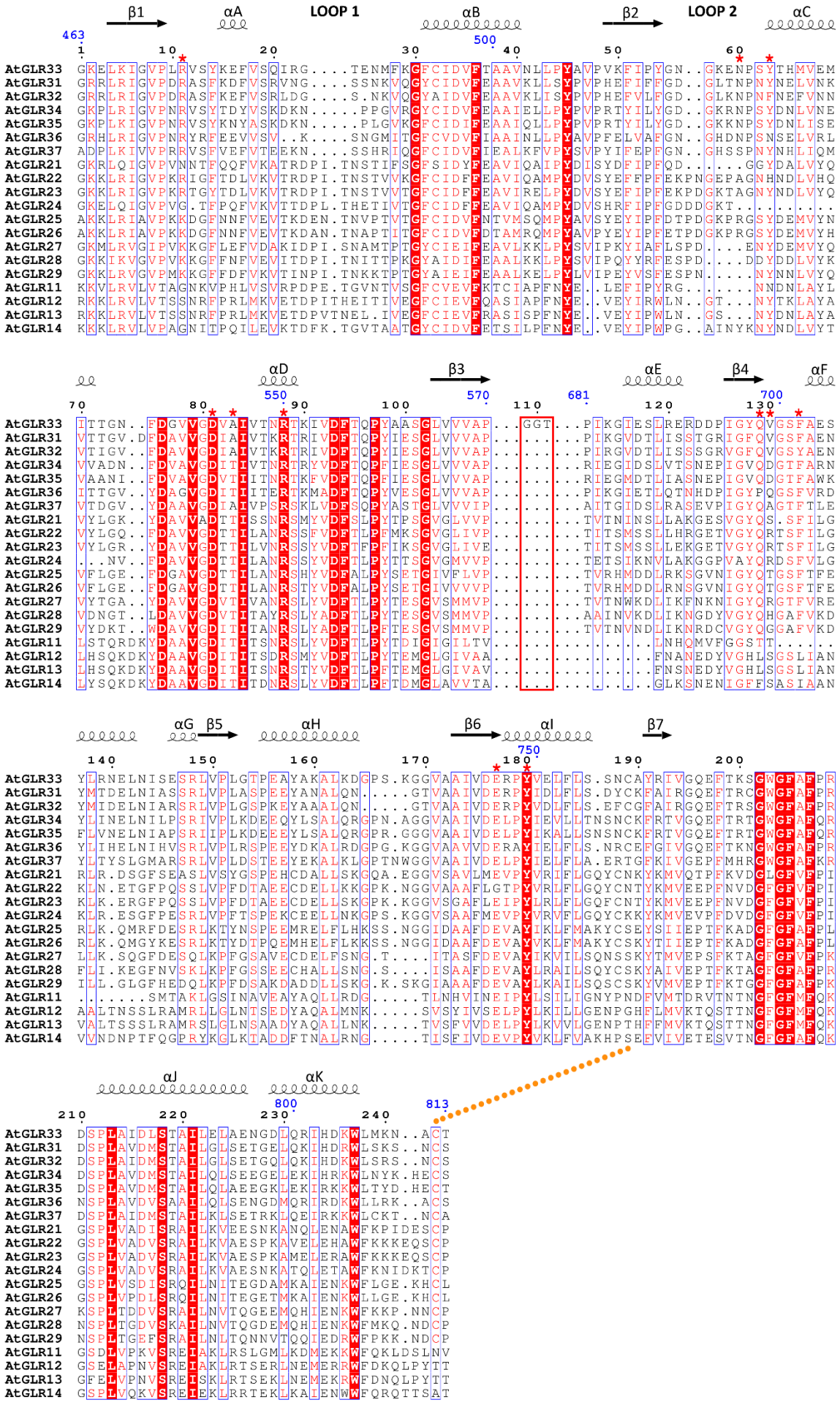
β1
αA
LOOP 1
αB
β2
LOOP 2
αC
αD
β3
αE
β4
αF
αG
β5
αH
β6
αI
β7
αJ
αK
AtGLR33
AtGLR31
AtGLR32
AtGLR34
AtGLR35
AtGLR36
AtGLR37
AtGLR21
AtGLR22
AtGLR23
AtGLR24
AtGLR25
AtGLR26
AtGLR27
AtGLR28
AtGLR29
AtGLR11
AtGLR12
AtGLR13
AtGLR14

(previous page)

Fig. S15. Sequence alignment of the LBDs (S1+S2 segments) of all *A. thaliana* GLR isoforms, with the GLR3.3 LBD sequence (this work) at the top and the other sequences grouped by clade. Above the alignment, the GLR3.3 secondary structure (α-helices as coils, β-strands as arrows), full-length numbering (blue) and numbering of the construct used in this paper (black) are shown. Location of the intervening M1-M2-M3 sequence (replaced by the GGT linker in the GLR3.3 construct of this work) is indicated by a red box. The position of the disulfide bond in GLR3.3 is indicated by orange dots. Residues involved in ligand binding in the GLR3.3 LBD structure are marked with red stars. See *SI Appendix*, Materials and Methods for the production of this alignment.

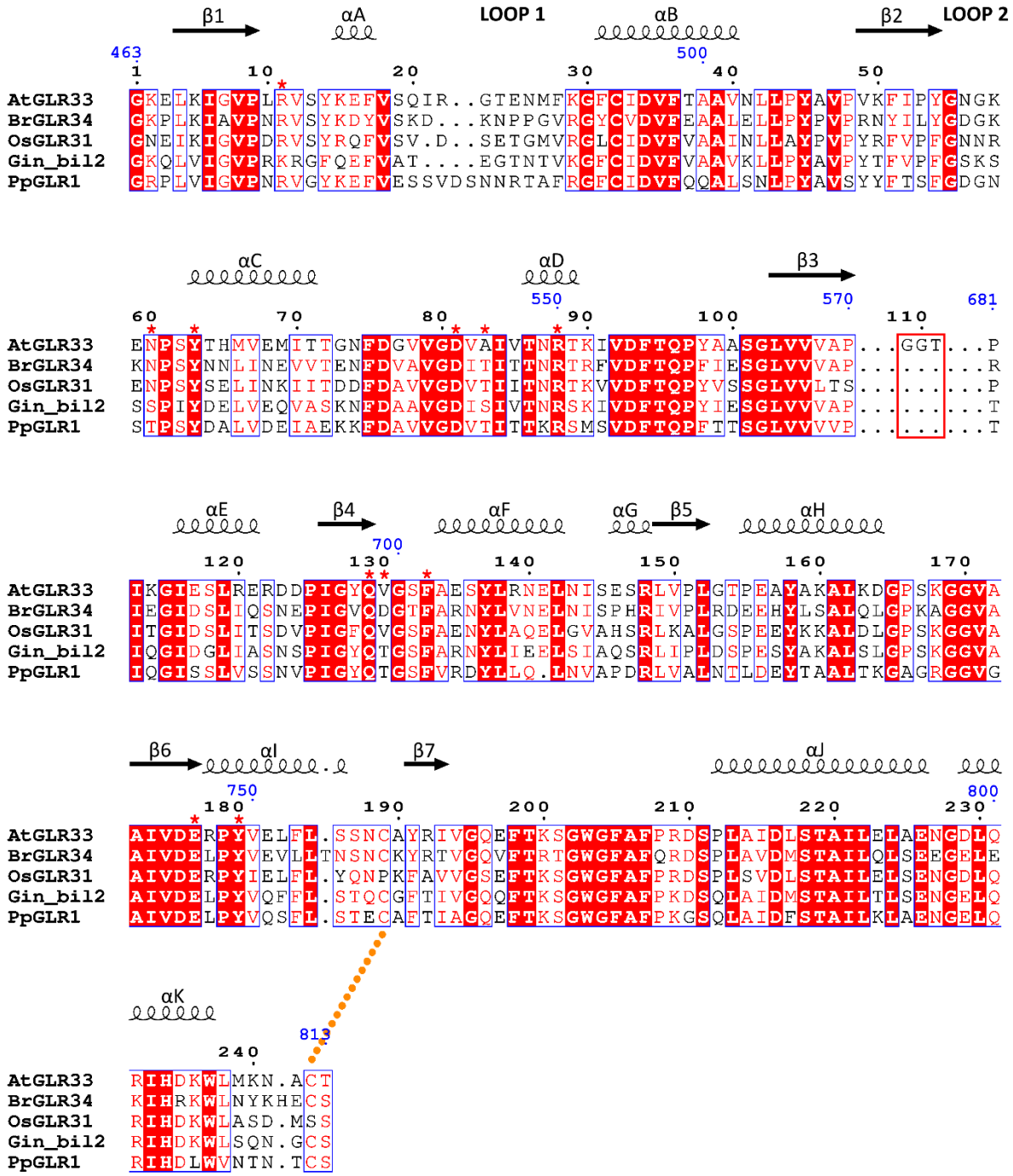

Fig. S16. Sequence alignment of LBDs (S1+S2 segments) of clade 3 GLRs from different plant species. *At*GLR3.3: *Arabidopsis thaliana* GLR3.3 (this work); *Br*GLR3.4: *Brassica rapa* GLR3.4; *Os*GLR3.1: *Oryza sativa* GLR3.1; Gin_bil2: *Ginkgo biloba* putative GLR2; *Pp*GLR1: moss *Physcomitrella patens* GLR1. At the top of the alignment, the *At*GLR3.3 secondary structure (α-helices as coils, β-strands as arrows), full-length numbering (blue) and numbering of the construct used in this paper (black) are shown. Location of the intervening M1-M2-M3 sequence (replaced by the GGT linker in the *At*GLR3.3 construct of this work) is indicated by a red box. The position of the disulphide bond in *At*GLR3.3 is indicated by orange dots. Residues involved in ligand binding in the *At*GLR3.3 LBD structure are marked with red stars. See *SI Appendix*, Materials and Methods for the production of this alignment.

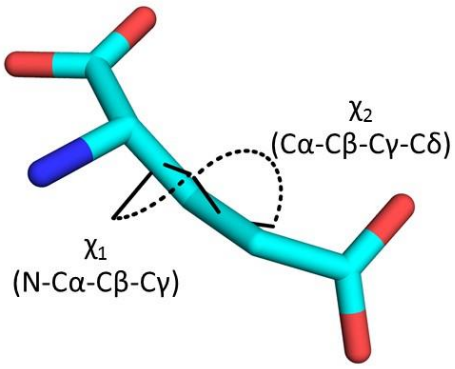

563

GLR/iGluR LBD	PDB ID	chain	χ_1 (°)	χ_2 (°)
Arabidopsis thaliana GLR3.3 (this work)	6r85	A	-81	-149
	6r85	B	-75	-151
Eukaryotes (non-plant)				
Rattus norvegicus GluA2 (AMPA-type)	1ftj	A	-78	-72
	1ftj	B	-76	-74
	1ftj	C	-73	-73
	3rn8	A	-74	-75
	3rn8	B	-76	-71
	3rn8	C	-75	-73
Rattus norvegicus GluA3 (AMPA-type)	3dln	A	-75	-75
Rattus norvegicus GluA4 (AMPA-type)	3epe	A	-75	-77
	3epe	B	-76	-71
Homo sapiens GluK1 (kainate-type)	2zns	A	-83	-67
Rattus norvegicus GluK2 (kainate-type)	1s50	A	-79	-67
Homo sapiens GluN2A (NMDA-type)	5h8f	A	-83	-60
Adineta vaga AvGluR1	4io2	A	-57	-70
	4io2	B	-59	-71
Drosophila melanogaster GluRIIB	4wxj	A	-73	-81
	4wxj	B	-70	-80
Drosophila melanogaster GluR1A	5dt6	A	-81	-70
Prokaryotes				
Synechocystis sp. GluR0	1ii5	A	-57	-179
Thermus thermophilus GluR0	1us5	A	-61	-177
Nostoc punctiforme GluR0	2pyy	A	-174	-175
	2pyy	B	-175	-174
	2pyy	C	-176	-178

564

565 **Fig. S17**. Table reporting the values (°) of the χ_1 and χ_2 dihedral angles of the L-Glu ligand side chain
566 for a number of deposited structures of glutamate-bound GLR/iGluR ligand-binding domains.

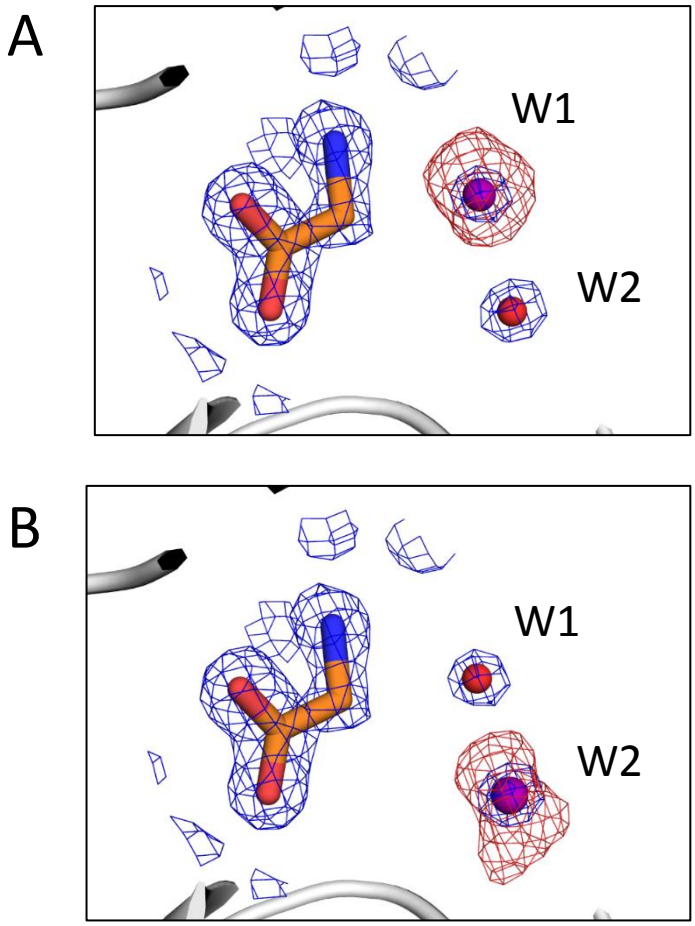

Fig. S18. Alternative refinement of GLR3.3 + Gly dataset. A Cl^- ion was placed in the position of either of the two additional water molecules in the Gly dataset ligand pocket and 5 cycles of restrained refinement were performed by the software *REFMAC5* (42); a clear peak of negative density in the $|\boldsymbol{F}|_o$-$|\boldsymbol{F}|_c$ electron density map (red mesh in the figure, showed at 3.0 σ contour level) appeared and the corresponding B-factors increased from 20.2 to 36.6 (W1 position) and from 21.9 to 37.3 (W2 position), ruling out the possibility that the spherical densities may correspond to ions rather than water molecules. Extending this operation to the four water molecules of the pocket in all chains of the Gly dataset invariantly causes increases of B-factors from a range of around 15-20 to a range of 37-60. The blue mesh corresponds to the $2|\boldsymbol{F}|_o$-$|\boldsymbol{F}|_c$ electron density map at 1.5 σ contour level.

Table S1. Crystallographic statistics. Values in parentheses are for the highest-resolution shell.

	SeMet +L-Glu	native +L-Glu	native +Gly	native +L-Cys	native +L-Met
Data collection					
Space group	$P4_32_12$	P1*	$P2_12_12_1$	$P2_12_12_1$	$P2_12_12_1$
Cell parameters (*a*,*b*,*c*, Å)	98.4, 98.4, 113.9	35.9, 61.3, 64.1	97.0, 98.2, 114.3	97.7, 98.5, 114.1	95.5, 96.8, 114.8
Cell parameters (α,β,γ, °)	90.0	75.2, 75.5, 90.0	90.0	90.0	90.0
Resolution (Å)	50.0-2.4	60.0-2.0	50.0-1.6	50.0-2.5	50.0-3.2
No. of monomers / asymm. unit	2	2	4	4	4
Observations	974572	105514	940331	260518	76068
Unique reflections	22542	33332	144028	38874	17844
R_{merge} [a]	0.28 (4.4)	0.10 (0.44)	0.07 (0.74)	0.25 (1.43)	0.42 (2.32)
Mean *I/σ(I)*	16.0 (1.2)	4.9 (1.6)	12.9 (1.7)	6.0 (1.1)	4.5 (1.4)
Completeness (%)	100.0 (99.8)	96.7 (94.7)	100.0 (100.0)	100.0 (100.0)	98.7 (99.6)
Multiplicity	43.2 (43.9)	3.2 (3.2)	6.5 (4.9)	6.7 (6.9)	4.3 (4.6)
Phasing					
Anomalous completeness (%)	100.0 (99.9)	-	-	-	-
Anomalous multiplicity	23.0 (22.8)	-	-	-	-
Overall FOM (centric/acentric) [b]	0.21 (0.09/0.23)	-	-	-	-
Refinement					
R-factor/R_{free} [c]		0.207/0.262	0.151/0.181	0.188/0.228	0.242/0.307
No. of protein residues / monomer		238;239	242;238;238;243	238;239;239;238	239;209;237;237**
Average B-factor (Å^2) [d]		24.1	21.2	38.1	39.7
No. of ligand molecules		2	4	4	4
Average B-factor (Å^2) [d]		17.2	16.5	37.7	32.1
No. of ions		4	8	3	2
Average B-factor (Å^2) [d]		34.4	46.2	46.9	17.5
No. of water molecules		315	1048	387	1
Average B-factor (Å^2) [d]		31.1	35.7	32.3	7.0
rmsd bond lengths (Å) [e]		0.007	0.013	0.007	0.006
rmsd bond angles (°) [e]		1.48	1.81	1.47	1.38
Ramachandran plot					
in preferred regions (%)		97.4	97.6	97.5	98.0
in allowed regions (%)		2.6	2.4	2.5	2.0
outliers (%)		0.0	0.0	0.0	0.0
MolProbity Score[f]		1.96 (76th percentile)	1.27 (97th percentile)	1.26 (100th percentile)	1.97 (99th percentile)
PDB ID		6R85	6R88	6R89	6R8A

* Data from native crystals +L-Glu solved in space group C2 (a=124.2, b=35.9, c=61.3; α=90.0, β=105.4, γ=90.0) showed slightly worse statistics; all statistics reported here for native crystals +L-Glu refer to data solved in space group P1.

** In the chain B of the L-Met dataset, a total of 29 internal residues were not included in the final PDB due to missing or very poor electron density.

[a] R-merge = $\Sigma_{hkl}\Sigma_j \mid I_{hkl,j} - \langle I_{hkl} \rangle \mid / \Sigma_{hkl}\Sigma_j I_{hkl,j}$.

The high R_{merge} value observed for the selenomethionine dataset and the L-Cys and L-Met datasets was due to the considerable redundancy of the dataset and/or a partial decay of the crystal during data collection. Maps calculated including all data were of higher quality than those calculated by including a largely redundant but more restricted subset of reflections with lower resolution and lower R_{merge}.

[b] Overall figure of merit (and for centric and acentric reflections) calculated by the program *Phaser* (53).

[c] R-factor = $\Sigma_{hkl} \mid Fobs_{hkl} - Fcalc_{hkl} \mid / \Sigma_{hkl} \mid Fobs_{hkl} \mid$ where Fobs and Fcalc are the observed and calculated structure factor amplitudes, respectively. R_{free} is the R-factor value for 5% of the reflections excluded from the refinement.

[d] Average B-factors calculated with the program Baverage from the *CCP4* suite (27).

[e] Root mean square deviations from ideal values calculated with *REFMAC5* (42).

[f] combines the clashscore, rotamer and Ramachandran evaluations giving one number that reflects the crystallographic resolution at which those values would be expected; from the server *MolProbity* (http://molprobity.biochem.duke.edu/) (45).

Table S2. Table listing the GLR3.3 LBD mutants generated and tested by small-scale expression in *E. coli*. The corresponding results are reported. Condition 1: induction by 1 mM IPTG followed by shaking at 37 °C for 3 h. Condition 2: induction by 0.1 mM IPTG followed by shaking at 20 °C for 16 h.

MUTANT	DESCRIPTION	CONDITION	EXPRESSION	SOLUBILITY	SCALE-UP
R88N	ligand-contacting residue	1	very good	very poor	no
		2	very good	very poor	no
R88N,Y63K	ligand-contacting residues	1	very good	very poor	no
		2	very good	very poor	no
R88K	ligand-contacting residue	1	very good	none	no
		2	very good	very poor	no
Y63K	ligand-contacting residue	1	very good	none	no
		2	good with degradation	very poor	no
D81G	residue from the outer network	1	very good	none	no
		2	very good	none	no
E177S	ligand-contacting residue	1	very good	none	no
		2	very good	none	no
E177S,Y180F	ligand-contacting residues	1	very good	none	no
		2	very good	very poor	no
S13A,Y14A	residues at domain interface	1	good	none	no
		2	good	good	yes

Table S3. Homology modelling statistics.

All models were generated using the online server SWISS-MODEL (swissmodel.expasy.org) (47). In all cases the areas affected by the lowest local reliability correspond to the exposed loop 1 (Fig. 2*A*), except for the *At*GLR1.4 LBD model, where all exposed loops have a low quality score.

Target protein	UniProtKB entry[a]	Araport identifier[b]	% id[c]	GMQE[d]	QMEAN Z-score[e]	MolProbity score[f]
AtGLR1.2 (LBD)	Q9LV72	AT5G48400	31.2	0.67	-2.32	2.14
AtGLR1.4 (LBD)	Q8LGN1	AT3G07520	32.1	0.65	-3.97	2.43
AtGLR3.1 (LBD)	Q7XJL2	AT2G17260	65.1	0.83	-0.42	1.56
AtGLR3.4 (LBD)	Q8GXJ4	AT1G05200	61.5	0.81	-0.95	1.82
AtGLR3.5 (LBD)	Q9SW97	AT2G32390	60.3	0.82	0.12	1.62

[a] UniProt: https://www.uniprot.org/

[b] Araport: https://www.araport.org/

[c] % sequence identity with GLR3.3 LBD

[d] Global Model Quality Estimation (number between 0 and 1) is a quality estimation which combines properties from the target–template alignment and coverage of the target.

[e] The QMEAN Z-score indicates how far the QMEAN score (54) of the model is from what one would expect from experimental structures of similar size. QMEAN Z-scores around zero indicate good agreement between the model structure and experimental structures of similar size. Scores of -4.0 or below indicate low quality of the model. The QMEAN score itself estimates global and local quality of geometry in one single model.

[f] Combines the clashscore, rotamer and Ramachandran evaluations giving one number that reflects the crystallographic resolution at which those values would be expected; from the server *MolProbity* (45).

SI REFERENCES

1. Krebs M, et al. (2012) FRET-based genetically encoded sensors allow high-resolution live cell imaging of Ca^{2+} dynamics. *Plant J* 69(1):181–192.
2. Costa A, Candeo A, Fieramonti L, Valentini G, Bassi A (2013) Calcium Dynamics in Root Cells of Arabidopsis thaliana Visualized with Selective Plane Illumination Microscopy. *PLoS One* 8(10):e75646.
3. Candeo A, Doccula FG, Valentini G, Bassi A, Costa A (2017) Light Sheet Fluorescence Microscopy Quantifies Calcium Oscillations in Root Hairs of Arabidopsis thaliana. *Plant Cell Physiol* 58(7):1161–1172.
4. Qi Z, Stephens NR, Spalding EP (2006) Calcium Entry Mediated by GLR3.3, an Arabidopsis Glutamate Receptor with a Broad Agonist Profile. *Plant Physiol* 142(3):963–971.
5. Tapken D, et al. (2013) A Plant Homolog of Animal Glutamate Receptors Is an Ion Channel Gated by Multiple Hydrophobic Amino Acids. *Sci Signal* 6(279):ra47. doi:10.1126/scisignal.2003762.
6. Stephens NR, Qi Z, Spalding EP (2007) Glutamate Receptor Subtypes Evidenced by Differences in Desensitization and Dependence on the GLR3.3 and GLR3.4 Genes. *Plant Physiol* 146(2):529–538.
7. Li F, et al. (2013) Glutamate Receptor-Like Channel3.3 Is Involved in Mediating Glutathione-Triggered Cytosolic Calcium Transients, Transcriptional Changes, and Innate Immunity Responses in Arabidopsis. *Plant Physiol* 162(3):1497–1509.
8. Vincill ED, Bieck AM, Spalding EP (2012) Ca^{2+} Conduction by an Amino Acid-Gated Ion Channel Related to Glutamate Receptors. *Plant Physiol* 159(1):40–46.
9. Nguyen CT, Kurenda A, Stolz S, Chételat A, Farmer EE (2018) Identification of cell populations necessary for leaf-to-leaf electrical signaling in a wounded plant. *Proc Natl Acad Sci* 115(40):10178–10183.
10. Wudick MM, et al. (2018) CORNICHON sorting and regulation of GLR channels underlie pollen tube Ca^{2+} homeostasis. *Science* 360(6388):533–536.
11. Brockie PJ, et al. (2013) Cornichons Control ER Export of AMPA Receptors to Regulate Synaptic Excitability. *Neuron* 80(1):129-42. doi: 10.1016/j.neuron.2013.07.028.
12. Cunningham KW, Fink GR (2015) Calcineurin inhibits VCX1-dependent H^+/Ca^{2+} exchange and induces Ca^{2+} ATPases in Saccharomyces cerevisiae. *Mol Cell Biol* 16(5):2226–2237.
13. Yadav AK, et al. (2015) A rice tonoplastic calcium exchanger, OsCCX2 mediates Ca^{2+}/cation transport in yeast. *Sci Rep* 5:1–15. doi:10.1038/srep17117.
14. Corso M, Doccula FG, de Melo JRF, Costa A, Verbruggen N (2018) Endoplasmic reticulum-localized CCX2 is required for osmotolerance by regulating ER and cytosolic Ca^{2+} dynamics in *Arabidopsis*. *Proc Natl Acad Sci* 115(15):3966–3971.
15. Clough SJ, Bent AF (1998) Floral dip: A simplified method for Agrobacterium-mediated transformation of Arabidopsis thaliana. *Plant J* 16(6):735–743.
16. Murashige T, Skoog F (1962) A revised medium for rapid growth and biosynthesis with tobacco tissue culture. *Physiol Plant* 15, 473–497. doi:10.1111/j.1399-3054.1962.tb08052.x
17. Behera S, Kudla J (2013) High-Resolution Imaging of Cytoplasmic Ca^{2+} Dynamics in

686 Arabidopsis Roots. *Cold Spring Harb Protoc* 8(7):670–674.

687 18. Armada NR, et al. (2019) In Vivo Light Sheet Fluorescence Microscopy of Calcium
688 Oscillations in Arabidopsis thaliana. Calcium Signalling: Methods and Protocols, Methods in
689 Molecular Biology, eds Raffaello A, Vecellio Reane D (Springer Nature, Heidelberg), vol.
690 1925, pp 87-101.

691 19. Maizel A, Von Wangenheim D, Federici F, Haseloff J, Stelzer EHK (2011) High-resolution live
692 imaging of plant growth in near physiological bright conditions using light sheet
693 fluorescence microscopy. *Plant J* 68(2):377–385.

694 20. Bonza MC, Luoni L, De Michelis MI (2004) Functional expression in yeast of an N-deleted
695 form of At-ACA8, a plasma membrane Ca^{2+}-ATPase of Arabidopsis thaliana, and
696 characterization of a hyperactive mutant. *Planta* 218(5):814–823.

697 21. Waterhouse AM, Procter JB, Martin DMA, Clamp M, Barton GJ (2009) Jalview Version 2 - A
698 multiple sequence alignment editor and analysis workbench. *Bioinformatics* 25(9):1189–
699 1191.

700 22. Doublié S (1997) Preparation of Selenomethionyl Proteins for Phase Determination.
701 *Methods Enzymol* 276:523–530. doi: 10.1016/S0076-6879(97)76075-0.

702 23. Jerabek-Willemsen M, et al. (2014) MicroScale Thermophoresis : Interaction analysis and
703 beyond. *J Mol Struct* 1077:101–113. doi:10.1016/j.molstruc.2014.03.009.

704 24. Scheuermann TH, Padrick SB, Gardner KH, Brautigam CA (2016) On the acquisition and
705 analysis of microscale thermophoresis data. *Anal Biochem* 496:79–93.
706 doi:10.1016/j.ab.2015.12.013.

707 25. Seidel SAI, et al. (2012) Label-free microscale thermophoresis discriminates sites and affinity
708 of protein-ligand binding. *Angew Chemie - Int Ed* 51(42):10656–10659.

709 26. Guijarro M, et al. (2012) ID29: a high-intensity highly automated ESRF beamline for
710 macromolecular crystallography experiments exploiting anomalous scattering. *J*
711 *Synchrotron Radiat* 19(3):455–461.

712 27. Winn MD, et al. (2011) Overview of the CCP4 suite and current developments. *Acta*
713 *Crystallogr Sect D Biol Crystallogr* 67(4):235–242.

714 28. Kabsch W (2010) XDS. *Acta Crystallogr Sect D Biol Crystallogr* 66(2):125–132.

715 29. Evans PR, Murshudov GN (2013) How good are my data and what is the resolution? *Acta*
716 *Crystallogr Sect D Biol Crystallogr* 69(7):1204–1214.

717 30. Karplus PA, Diederichs K (2012) Linking crystallographic model and data quality. *Science*
718 336(6084):1030–1033.

719 31. Altschul SF, et al. (1997) Gapped BLAST and PSI-BLAST: A new generation of protein
720 database search programs. *Nucleic Acids Res* 25(17):3389–3402.

721 32. Rychlewski L, Li W, Jaroszewski L, Godzik A (2010) Comparison of sequence profiles.
722 Strategies for structural predictions using sequence information. *Protein Sci* 9(2):232–241.

723 33. Schuermann JP, Tanner JJ (2003) MRSAD: Using anomalous dispersion from S atoms
724 collected at Cu Kα wavelength in molecular-replacement structure determination. *Acta*
725 *Crystallogr - Sect D Biol Crystallogr* 59(10):1731–1736.

726 34. Panjikar S, Parthasarathy V, Lamzin VS, Weiss MS, Tucker PA (2009) On the combination of

molecular replacement and single-wavelength anomalous diffraction phasing for automated structure determination. *Acta Crystallogr Sect D Biol Crystallogr* 65(10):1089–1097.

35. Potterton L, et al. (2018) CCP4i2: The new graphical user interface to the CCP4 program suite. *Acta Crystallogr Sect D Struct Biol* 74:68–84. doi:10.1107/S2059798317016035.

36. Skubák P, Pannu NS (2013) Automatic protein structure solution from weak X-ray data. *Nat Commun* 4:1–6. doi:10.1038/ncomms3777.

37. Cowtan K (2006) The Buccaneer software for automated model building. 1. Tracing protein chains. *Acta Crystallogr Sect D Biol Crystallogr* 62(9):1002–1011.

38. Bricogne G, Blanc E, Brandl M, Flensburg C, Keller P, Paciorek W, Roversi P, Sharff A, Smart OS, Vonrhein C, Womack TO (2017). BUSTER version 2.10.2. Cambridge, United Kingdom: Global Phasing Ltd.

39. Blanc E, et al. (2004) Refinement of severely incomplete structures with maximum likelihood in BUSTER-TNT. *Acta Crystallogr Sect D Biol Crystallogr* 60(12 I):2210–2221. doi:10.1107/S0907444904016427.

40. Adams PD, et al. (2010) PHENIX: A comprehensive Python-based system for macromolecular structure solution. *Acta Crystallogr Sect D Biol Crystallogr* 66(2):213–221.

41. Vagin A, Teplyakov A (2010) Molecular replacement with MOLREP. *Acta Crystallogr Sect D Biol Crystallogr* 66(1):22–25.

42. Murshudov GN, et al. (2011) REFMAC5 for the refinement of macromolecular crystal structures. *Acta Crystallogr Sect D Biol Crystallogr* 67(4):355–367.

43. Emsley P, Lohkamp B, Scott WG, Cowtan K (2010) Features and development of Coot . *Acta Crystallogr Sect D Biol Crystallogr* 66(4):486–501.

44. Morris RJ, Perrakis A, Lamzin VS (2003) ARP/wARP and automatic interpretation of protein electron density maps. *Methods Enzymol* 374:229-44. doi: 10.1016/S0076-6879(03)74011-7.

45. Chen VB, et al. (2010) MolProbity: All-atom structure validation for macromolecular crystallography. *Acta Crystallogr Sect D Biol Crystallogr* 66(1):12–21.

46. Strong M, et al. (2006) Toward the structural genomics of complexes: Crystal structure of a PE/PPE protein complex from Mycobacterium tuberculosis. *Proc Natl Acad Sci* 103(21):8060–8065.

47. Waterhouse A, et al. (2018) SWISS-MODEL: homology modelling of protein structures and complexes. *Nucleic Acids Res* 46(W1):W296–W303.

48. Tian W, Chen C, Lei X, Zhao J, Liang J (2018) CASTp 3.0: Computed atlas of surface topography of proteins. *Nucleic Acids Res* 46(W1):W363–W367.

49. Sievers F, et al. (2011) Fast, scalable generation of high-quality protein multiple sequence alignments using Clustal Omega. *Mol Syst Biol* 7:539. doi: 10.1038/msb.2011.75.

50. Robert X, Gouet P (2014) Deciphering key features in protein structures with the new ENDscript server. *Nucleic Acids Res* 42(W1):320–324.

51. De Bortoli S, Teardo E, Szabò I, Morosinotto T, Alboresi A (2016) Evolutionary insight into the ionotropic glutamate receptor superfamily of photosynthetic organisms. *Biophys Chem* 218:14–26. doi:10.1016/j.bpc.2016.07.004.

52. Twomey EC, Yelshanskaya M V., Grassucci RA, Frank J, Sobolevsky AI (2016) Elucidation of AMPA receptor-stargazin complexes by cryo-electron microscopy. *Science* 353(6294):83–86.

53. McCoy AJ, et al. (2007) Phaser crystallographic software. *J Appl Crystallogr* 40(4):658–674.

54. Benkert P, Biasini M, Schwede T (2011) Toward the estimation of the absolute quality of individual protein structure models. *Bioinformatics* 27(3):343–350.